Proton hot spots and exclusive vector meson production

S. Demirci,[1,2] T. Lappi,[1,2] and S. Schlichting[3]

[1]*Department of Physics, University of Jyväskylä, P.O. Box 35, Jyväskylä 40014, Finland*
[2]*Helsinki Institute of Physics, University of Helsinki, P.O. Box 64, Helsinki 00014, Finland*
[3]*Fakultät für Physik, Universität Bielefeld, D-33615 Bielefeld, Germany*

(Received 27 July 2022; accepted 29 September 2022; published 28 October 2022)

We explore consequences of the existence of gluonic hot spots inside the proton for coherent and incoherent exclusive vector meson production cross sections in deep inelastic scattering. By working in the dilute limit of the Color Glass Condensate framework to compute the cross sections for Gaussian hot spots of fluctuating color charges and employing a nonrelativistic vector meson wave function, we are able to perform large parts of the calculation analytically. We find that the coherent cross section is sensitive to both the size of the target and the structure of the probe. The incoherent cross section is dominated by color fluctuations at small transverse momentum transfer (t), by proton and hot spot sizes as well as the structure of the probe at medium t and again by color fluctuations at large t. While the t-dependence of the cross section is well reproduced in our model, the relative normalization between the coherent and the incoherent cross sections points to the need for additional fluctuations in the proton.

DOI: 10.1103/PhysRevD.106.074025

I. INTRODUCTION

Understanding the structure of the proton in terms of its fundamental quark and gluon constituents is an ever-important question in high-energy physics. Since the proton is a composite bound state of QCD, its partonic structure is, in general, nonperturbative and can only be accessed within nonperturbative calculations, e.g., in lattice QCD, or extracted from experiments. One of the cleanest ways to study this structure experimentally is by deeply inelastic $e+p$ scattering (DIS) experiments. Perhaps the most widely used experimental data comes from the H1 and ZEUS experiments performed at the Hadron-Electron Ring Accelerator (HERA) [1–5]. Currently, the active experimental program of ultraperipheral, photon mediated, interactions [6,7] at the LHC and RHIC also gives clean access to proton structure via $\gamma+p$ collisions. In the future, a much more detailed picture of the structure of the proton will be reached with the Electron-Ion Collider (EIC) [8–10].

For a long time it has been standard to describe the proton in terms of collinear parton distribution functions (PDFs), which describe the (longitudinal) momentum distributions of partons inside the proton. However, in recent years it has become increasingly well understood that the (transverse) spatial distribution of partons in the proton can also have a significant impact on hadron production in $p-p$ and $p-Pb$ collisions [11–23]. In particular, experimental observations of so-called collective flow of soft hadrons in $p+p$ and $p+Pb$ collisions provide a strong motivation to study the (transverse) spatial distribution of partons in the proton.

A common approach to the internal transverse coordinate structure that is frequently employed in phenomenological studies of $p-p$ and $p-Pb$ collisions is based on a picture of the proton consisting of a certain number of gluonic "hot spots" [13,20–28]. Evidently, such a model is motivated by the valence quark picture of the proton, from which one can conjecture that perhaps most of the partons in the proton should be close to these valence quarks, which ultimately are the source of the smaller-x ones (see Refs. [29,30] for a recent explicit realization of this idea). For a review on proton and nuclear shape fluctuations see [18].

Our aim in this paper is to understand to what extent one can probe and constrain different aspects of such a hot spot model using $e+p\to e+p^{(*)}+V$ exclusive vector meson (V) production cross sections in DIS. To this end we use the formulation of the hot spot model from our previous work [26], which shares the basic physics ingredients with several hot spot models recently used in the literature, see e.g., Refs. [20–22,24,25]. Our approach leads to a simple, analytically tractable model for the cross sections which includes different sources of fluctuations in the subnucleon degrees of freedom inside the proton. By exploiting this analytic approach, our aim is to understand

how much one can actually learn about the impact parameter dependent structure of the proton independently of the properties of the probe in exclusive vector meson production.

The starting point for our approach is the Color Glass Condensate (CGC) formalism [31] to describe the partonic structure of the high-energy proton. In this framework the large-x partons act as color charges which produce the small-x gluons. These dominate the small-x part of the proton and are taken to be sufficiently dense to be described by classical color fields. The correlations of the color charges are taken to be Gaussian as in the McLerran-Venugopalan (MV) model [32–34]. In this work we assume the proton to be dilute meaning that we expand the operators defining the observables into the lowest nontrivial order in the field strength, akin to the leading order in the twist expansion.

In our model [26] a nontrivial spatial structure of the proton emerges, as the large-x color charges of the proton are taken to be distributed into hot spots. These hot spots have a Gaussian shape and are statistically distributed according to a Gaussian distribution, in such a way that the center of mass is at the center of the proton. Nevertheless, the locations of individual hot spots fluctuate from event to event and have to be averaged over to calculate the cross section. By taking into consideration the number of valence quarks, which generally carry a large fraction of the proton momentum and are thus part of the CGC color charge, it would be natural to assume that the number of hot spots would be $N_q = 3$. However, this is not a necessity as the valence quarks can also emit large-x gluons, which can proceed and emit other large-x partons. Such kind of processes could increase the number of hot spots in the proton, and it is also conceivable that the number of hot spots fluctuates on event-by-event basis. Within our work we allow the number of hot spots (N_q) to be a free parameter in our calculations until the numerical analysis, but we do not take into account event-by-event fluctuations of the number of hot spots (N_q).

We combine our hot spot model with other commonly used physics ingredients to calculate exclusive vector meson production cross sections in $\gamma^{(*)}p$ collisions. The scattering process is modelled using the dipole picture [35]. In this picture the incoming photon fluctuates into a quark-antiquark dipole which interacts with the classical color field of the proton, after which the dipole forms a vector meson. This calculation requires the use of a photon and a vector meson wave function, or more specifically the overlap of the two [35]. We take the vector meson wave function to be nonrelativistic to make the model as simple and the calculation as analytically tractable as possible. We use the nonrelativistic wave function from Ref. [36].

The dipole picture naturally has an impact parameter dependence. This makes it a good way to understand the transverse structure of the target proton. The impact parameter is the Fourier conjugate of the Mandelstam variable t, which describes the squared momentum change of the proton, approximated to be purely transverse due to the high energy nature of the collision. This means that larger transverse momentum transfers probe smaller size-structures inside the proton.

When the virtuality of the photon or the mass of the quark in the dipole is large, the photon wave function greatly favors small dipole sizes. This is an approximation one might use when computing J/Ψ exclusive vector meson production cross sections. We will study how good this approximation actually is in our model. For this reason we study processes where the dipole consists of a $c\bar{c}$, $b\bar{b}$ or $t\bar{t}$ pairs. The first two are phenomenologically relevant and the last acts as the true nonrelativistic limit and is studied as a way to give a reference point for the other two cases.

We use the Good-Walker [37,38] framework to compute coherent (target proton remains intact) and incoherent (target proton dissociates) exclusive vector meson production cross sections, both of which have been measured experimentally at HERA. The coherent cross section is proportional to the square of the average of the scattering amplitude [35]. This means that it is sensitive to the averages of the hot spot and color field fluctuations. The sum of the coherent and incoherent cross sections is proportional to the average of the square of the scattering amplitude [18,38,39]. Now because the incoherent cross section is the difference of the two, it is sensitive to the fluctuations in the scattering amplitude. In our work the sources for fluctuations are the event-by-event fluctuations of the color field of the proton and the fluctuating positions of the hot spots. Both of these two sources of fluctuations are averaged over analytically in the dilute limit for the proton. We study different contributions to the incoherent cross section separately to see how different features of the cross section are sensitive to different properties of the target, and to what extent they are independent of the probe.

The paper is organized as follows. First we briefly review the dipole picture for exclusive vector meson production in Sec. II A and the photon and vector meson wave function overlap needed for the scattering amplitude in Sec. II B. Next we recall in Sec. II C the basic properties of the hot spot model that we developed in Ref. [26] and discuss how the color and hot spot averages of the dipole cross section and its square are computed in Sec. II D. Subsequently we compute the coherent and incoherent exclusive vector meson production cross sections and separate the color and hot spot fluctuation parts of the incoherent cross section in Sec. II E. Next we discuss our results, present numerical evaluations of the cross sections and explain how our model depends on different parameters in Sec. III. We finish with a brief summary of our most important findings and conclusions in Sec. IV. In the appendixes we discuss the computation of the scattering amplitude averages in

more detail, and also study the small dipole size approximation and the asymptotic behavior of the cross section in different limits.

II. THEORETICAL FRAMEWORK

A. Exclusive vector meson production in the dipole picture

We describe exclusive vector meson production in the dipole picture using the Color Glass Condensate (CGC) formalism. In this picture, at the lowest order, the incoming virtual photon fluctuates into a quark-antiquark dipole which interacts with the color field of the proton. After the scattering the dipole forms the vector meson in the final state of the interaction, which can still decay before it is measured by a detector.

The scattering amplitude for the exclusive production of a transversely (T) or longitudinally (L) polarized vector meson can be expressed as [18,35]

$$\mathcal{A}_{T,L}^{\gamma^* p\to Vp}(Q^2,\Delta) = i\int d^2\mathbf{r}\int d^2\mathbf{b}\int\frac{dz}{4\pi}(\Psi^*\Psi_V)_{T,L}(Q^2,\mathbf{r},z) \times\exp\left\{-i\left[\mathbf{b}+\left(\frac{1}{2}-z\right)\mathbf{r}\right]\cdot\Delta\right\}\frac{d\sigma_{\mathrm{dip}}^{\mathrm{p}}}{d^2\mathbf{b}}(\mathbf{b},\mathbf{r}). \quad (1)$$

Here $\mathbf{b}$ refers to the impact parameter of the dipole with respect to the target proton, $\mathbf{r}$ is the transverse size vector of the dipole, Q^2 is the virtuality of the photon and z is the fraction of the plus component of the light cone momentum of the photon carried by the quark in the dipole. The transverse momentum transfer to the target is denoted by Δ, which according to Eq. (1) is the Fourier conjugate to $\mathbf{b}+(\frac{1}{2}-z)\mathbf{r}$.[1] The kinematic variables are visualized in the Fig. 1.

By using the Good-Walker [37–39,42,43] picture for fluctuations in the target, the coherent cross section can be written as a square of the average of the amplitude [35]

$$\frac{d\sigma_{T,L}^{\gamma^* p\to Vp}}{dt} = \frac{1}{16\pi}|\langle\!\langle\mathcal{A}_{T,L}^{\gamma^* p\to Vp}(Q^2,\Delta)\rangle\!\rangle|^2, \quad (2)$$

whereas the incoherent cross section can be written as the variance of the scattering amplitude as [18,38,39,43]

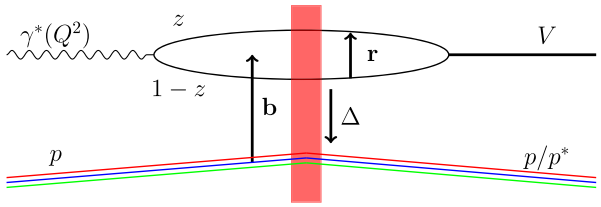

FIG. 1. Illustration of the scattering process with an incoming photon, target proton and its color field and the outgoing vector meson. The relevant kinematic variables have been shown in the figure. The virtuality of the incoming photon γ^* is Q^2, p/p^* is the proton/dissociated proton, z is the fraction of the photon momentum carried by the quark (or antiquark), V is the outgoing vector meson, $\mathbf{r}$ is the size of the dipole, $\mathbf{b}$ is the impact parameter of the dipole, Δ is the momentum transfer between the dipole and the proton system and the red rectangle represents the classical color field of the proton.

$$\frac{d\sigma_{T,L}^{\gamma^* p\to Vp^*}}{dt} = \frac{1}{16\pi}(\langle\!\langle|\mathcal{A}_{T,L}^{\gamma^* p\to Vp}(Q^2,\Delta)|^2\rangle\!\rangle - |\langle\!\langle\mathcal{A}_{T,L}^{\gamma^* p\to Vp}(Q^2,\Delta)\rangle\!\rangle|^2). \quad (3)$$

While the wave function overlap $(\Psi^*\Psi_V)_{T,L}(Q^2,\mathbf{r},z)$ characterizes the properties of the probe, the information on the target color fields is contained in what is called the dipole cross section, $\frac{d\sigma_{\mathrm{dip}}^{\mathrm{p}}}{d^2\mathbf{b}}(\mathbf{b},\mathbf{r})$. Hence, the computation of exclusive vector meson cross sections can be separated into computing the expectation value and variance of the dipole cross section in the proton hot spot model on one hand, and computing the wave function overlap $(\Psi^*\Psi_V)_{T,L}(Q^2,\mathbf{r},z)$ describing the overlap of the dipole with the (virtual) photon and vector meson states on the other hand. We will first discuss the latter one, before moving to the calculation of the dipole cross section in the hot spot model of Ref. [26].

B. Wave function overlap in the nonrelativistic limit

Within this study we will employ the leading order photon wave functions along with the strict nonrelativistic limit for the vector meson wave function to compute their overlap. Below we provide the relevant expressions, separately for the transverse and longitudinal polarizations. We first recall that the definition of the overlap is [35]

$$(\Psi_V^*\Psi_\gamma)_T = \frac{1}{2}\sum_{\substack{\lambda=+1,-1\\ h,h'=+,-}}(\Psi_{V,hh'}^{\lambda})^*\Psi_{\gamma,hh'}^{\lambda}$$
$$(\Psi_V^*\Psi_\gamma)_L = \sum_{h,h'=+,-}(\Psi_{V,hh'}^{\lambda=0})^*\Psi_{\gamma,hh'}^{\lambda=0}, \quad (4)$$

where h, h' refer to the helicities of the two quarks in the dipole and where λ refers to the polarization of the photon. The longitudinally and transversely polarized photon wave functions read [36]

[1]Note Eq. (1) contains the corrected phase factor [40,41] $(\frac{1}{2}-z)\mathbf{r}\cdot\Delta$ (instead of the $(1-z)\mathbf{r}\cdot\Delta$ that has been used in e.g., [35] and several other previous works). However, the $\mathbf{r}$ dependent phase factor does not influence the final results much [18] and will in fact completely vanish in the nonrelativistic limit, where the light cone momentum fraction is fixed to $z=1/2$, which we use in the following.

$$\Psi^{\lambda=0}_{\gamma,hh'}(z,|\mathbf{r}|) = -e_Q e\sqrt{N_c}\delta_{h,-h'}2Qz(1-z)\frac{K_0(\varepsilon|\mathbf{r}|)}{2\pi} \quad (5)$$

and

$$\Psi^{\lambda=\pm1}_{\gamma,hh'}(z,|\mathbf{r}|) = -e_Q e\sqrt{2N_c}\left[m_Q\frac{K_0(\varepsilon|\mathbf{r}|)}{2\pi}\delta_{h\pm}\delta_{h'\pm} \pm ie^{\pm i\theta_{\mathbf{r}}}\frac{\varepsilon K_1(\varepsilon|\mathbf{r}|)}{2\pi}(z\delta_{h\pm}\delta_{h'\mp}-(1-z)\delta_{h\mp}\delta_{h'\pm})\right], \quad (6)$$

where

$$\varepsilon = \sqrt{Q^2z(1-z)+m_Q^2}. \quad (7)$$

Here $e=\sqrt{4\pi\alpha_{\mathrm{em}}}$ denotes the electric charge, and e_Q refers to the fractional charge of the quark, i.e., $e_c=e_t=\frac{2}{3}$ for charm (c) and top (t) quarks and $e_b=-\frac{1}{3}$ for bottom (b) quarks.

In the nonrelativistic limit, the nonvanishing components of the vector meson wave function are given by [36]

$$\Psi^{\lambda=0}_{V,+-}(z,|\mathbf{r}|) = \Psi^{\lambda=0}_{V,-+}(z,|\mathbf{r}|) = A_Q\frac{\sqrt{2}\pi}{\sqrt{m_Q}}\delta\left(z-\frac{1}{2}\right) \quad (8)$$

and

$$\Psi^{\lambda=1}_{V,++}(z,|\mathbf{r}|) = \Psi^{\lambda=-1}_{V,--}(z,|\mathbf{r}|) = A_Q\frac{2\pi}{\sqrt{m_Q}}\delta\left(z-\frac{1}{2}\right), \quad (9)$$

where m_Q refers to the mass of the nonrelativistic heavy quark. The constant A_Q can be found from the leptonic decay width of the vector meson, which can be calculated from the same light cone wave function. Specifically for the $c\bar{c}$ case, the numerical value can be obtained from the decay width of the J/Ψ as [36]

$$\Gamma(J/\Psi\to e^-e^+) = A_c^2\frac{4\pi e_c^2\alpha_{\mathrm{em}}}{m_c^2}. \quad (10)$$

Using the experimental leptonic decay width the value of A_c is found in Ref. [36] to be

$$A_c = 0.211\ \mathrm{GeV}^{\frac{3}{2}}. \quad (11)$$

When studying the cases with different quark masses, we do not want to introduce uncertainties related to the decay constants into our calculation. Thus for heavier mesons we always compare cross sections divided by the leptonic decay widths, which cancels the constant A_Q.

By combining Eqs. (5), (6), (8), and (9), one can then compute the overlaps of the wave functions as

$$(\Psi_V^*\Psi_\gamma)_T = -A_Q\sqrt{2m_QN_c}e_Qe K_0(\varepsilon|\mathbf{r}|)\delta\left(z-\frac{1}{2}\right) \quad (12)$$

and

$$(\Psi_V^*\Psi_\gamma)_L = -A_Q\sqrt{\frac{2N_c}{m_Q}}2e_Qe Qz(1-z)K_0(\varepsilon|\mathbf{r}|)\delta\left(z-\frac{1}{2}\right), \quad (13)$$

which can be employed directly in the calculation of the exclusive vector meson production cross sections.

C. The hot spot model

We use the hot spot model formulated in Ref. [26] to quantify the event-by-event fluctuations of the structure of the proton. Within this model, an expectation value averaged over target fluctuations can be computed as a double average over the positions $\mathbf{b}_i$ of $i=1,\ldots,N_q$ hot spots inside the proton on the one hand, and individual realizations of color charges $\rho_a(\mathbf{x})$ inside the hot spots on the other hand. Event-by-event fluctuations of the proton structure thus consist of both color charge fluctuations as well as hot spot location fluctuations, and we will separately investigate the effects of both sources of fluctuations on the incoherent cross section.

Within the CGC description, the partons in the proton are divided into large-x color charges acting as sources for small-x classical gluon fields. Hence, it is natural to express the hot spot structure of the proton in terms of the impact parameter dependence of the color charge density $\rho_a(\mathbf{x})$, which vanishes on average $\langle\rho_a(\mathbf{x})\rangle_{\mathrm{CGC}}=0$ to satisfy color neutrality, but fluctuates on an event by event basis. Specifically, we consider the color charge density $\rho_a(\mathbf{x})$ to be concentrated around the location $\mathbf{b}_i$ of the hot spots, such that fluctuations of the color charge density are determined by

$$\langle\rho^a(\mathbf{x})\rho^b(\mathbf{y})\rangle_{\mathrm{CGC}} = \sum_{i=1}^{N_q}\mu^2\left(\frac{\mathbf{x}+\mathbf{y}}{2}-\mathbf{b}_i\right)\delta^{(2)}(\mathbf{x}-\mathbf{y})\delta^{ab}, \quad (14)$$

where $\mu^2(\mathbf{x})$ denotes the transverse profile of the hot spot, and following the MV model [32–34] we take the correlations of the color charges at different transverse points to be independent. We take a Gaussian profile for the hot spots in transverse coordinate space

$$\mu^2(\mathbf{x}) = \frac{\mu_0^2}{2\pi r_H^2}\exp\left[-\frac{\mathbf{x}^2}{2r_H^2}\right], \quad (15)$$

where r_H is the radius of the hot spot and μ_0^2 is a parameter describing the amount of color charge in the hot spot.

We note that the normalization in Eq. (15) is such that the dimensions of $\mu^2(\mathbf{x})$ and μ_0^2 are different.

By performing the CGC average of the correlation functions of the color charge density $\rho_a(\mathbf{x})$, the model thus accounts for color charge fluctuations inside the proton. When performing these averages, we will assume Gaussian statistics for the color charges as in the MV model [32–34]. This means that the CGC averages of higher order correlators such as $\langle \rho^a(\mathbf{x})\rho^b(\mathbf{y})\rho^c(\mathbf{x}')\rho^d(\mathbf{y}')\rangle_{\mathrm{CGC}}$, can be expressed in terms of the two-point function in Eq. (14) using Wick's theorem.

The spatial positions of the hot spots fluctuate on an event-by-event basis, and the distribution of the hot spot positions in the transverse plane is taken to be Gaussian

$$T(\mathbf{b}) = \frac{1}{2\pi R^2}\exp\left[-\frac{\mathbf{b}^2}{2R^2}\right]. \tag{16}$$

where R characterizes the size of the proton. By following our previous paper [26] the averages over the positions of the hot spots and the color charge fluctuations around the hot spots can be combined into a *double average*, such that the expectation value of an observable $\mathcal{O}$ is determined by

$$\langle\langle \mathcal{O} \rangle\rangle = \left(\frac{2\pi R^2}{N_q}\right)\int \prod_{i=1}^{N_q}[\mathrm{d}^2\mathbf{b}_i T(\mathbf{b}_i - \mathbf{B})] \times \delta^{(2)}\left(\frac{1}{N_q}\sum_{i=1}^{N_q}\mathbf{b}_i - \mathbf{B}\right)\langle \mathcal{O}\rangle_{\mathrm{CGC}}, \tag{17}$$

where, as illustrated in Fig. 2, N_q is the number of hot spots, $\mathbf{b}_i$ is the center of the ith hot spot and $\mathbf{B}$ is the center of mass of the proton. The prefactor is chosen in such a way that the double average is normalized, i.e., $\langle\langle 1\rangle\rangle = 1$. We note that the δ constraint in Eq. (17) fixes the center of mass of the hot spot system $\frac{1}{N_q}\sum_{i=1}^{N_q}\mathbf{b}_i$ to the center of mass of the proton $\mathbf{B}$. This procedure does not take into account the color charge fluctuations, but we believe that they give a much smaller contribution to it than the hot spot fluctuations. Since in this work the proton acts as a target for a dipole probe, we can further set $\mathbf{B} = 0$ without loss of generality and instead let the impact parameter of the dipole change.

We finally note that very similar hot spot models have been used in a variety of studies. In particular our model has most of the same physics ingredients and parameters as the so called IP-Glasma model [19,20]. The averaging over hot spot configurations and color charges in the IP-Glasma model is performed numerically by a Monte Carlo procedure. In our work we take the dilute limit in the color charges of the proton, which allows us to perform the averages analytically. In addition to taking the dilute limit, we also do not include the so called Q_s fluctuations in our model which were used in Ref. [20] by letting the saturation scale of each hot spot fluctuate independently. We also do not have repulsion between individual hot spots as in Refs. [13,28].

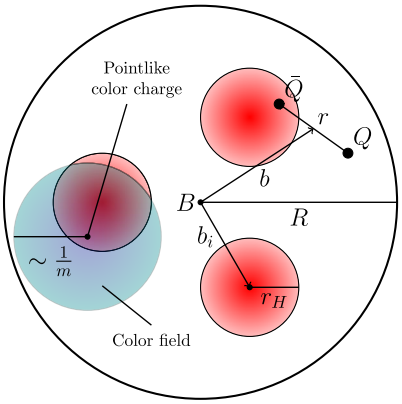

FIG. 2. The transverse profile of a hot spot model proton with a dipole probe. The red circles represent the hot spots containing the large-x color charges of the proton. The blue circle represents the classical color field of small-x gluons generated by a pointlike color charge within the hot spot. The other quantities are as follows: $\mathbf{B}$ is the center of mass of the proton, $\mathbf{b}_i$ is the position of the center of the ith hot spot, r_H is the radius of a hot spot, R is the radius parameter of the proton. The quark and antiquark forming the dipole are denoted by $Q(\bar{Q})$. The impact parameter of the dipole (with respect to the center of mass of the target) is denoted by $\mathbf{b}$, and $\mathbf{r}$ is the size of the dipole.

D. Average of the dipole cross section and its square

Next we proceed to calculate the two quantities

$$\left\langle\left\langle \frac{d\sigma_{\mathrm{dip}}^{\mathrm{p}}}{d^2\mathbf{b}}(\mathbf{b},\mathbf{r})\right\rangle\right\rangle \quad \text{and} \quad \left\langle\left\langle \frac{d\sigma_{\mathrm{dip}}^{\mathrm{p}}}{d^2\mathbf{b}}(\mathbf{b},\mathbf{r})\frac{d\sigma_{\mathrm{dip}}^{\mathrm{p}}}{d^2\bar{\mathbf{b}}}(\bar{\mathbf{b}},\bar{\mathbf{r}})\right\rangle\right\rangle, \tag{18}$$

as well as their Fourier transforms, where the double average now refers to averaging over both the color fields and the hot spot positions of the proton as discussed above.

The starting point of the calculation is the operator expression for the dipole cross section, which is given by twice the forward elastic scattering amplitude for a color neutral dipole to scatter off the target color field

$$\frac{d\sigma_{\mathrm{dip}}^{\mathrm{p}}}{d^2\mathbf{b}}(\mathbf{b},\mathbf{r}) = 2N(\mathbf{b},\mathbf{r}). \tag{19}$$

The dipole scattering amplitude $N(\mathbf{b},\mathbf{r})$ is obtained from the target color fields as a two-point function of Wilson lines

$$N(\mathbf{b},\mathbf{r}) = 1 - \frac{1}{N_c}\mathrm{Tr}[V(\mathbf{x})V^\dagger(\mathbf{y})], \tag{20}$$

where the (anti)quark transverse positions $(\mathbf{x},\mathbf{y})$ are connected to the dipole impact parameter $(\mathbf{b})$ and dipole radius $(\mathbf{r})$ coordinates $(\mathbf{b},\mathbf{r})$ by the transformations

$$\mathbf{b} = \frac{\mathbf{x}+\mathbf{y}}{2}, \qquad \mathbf{r} = \mathbf{x}-\mathbf{y} \tag{21}$$

or equivalently

$$\mathbf{x} = \mathbf{b} + \frac{\mathbf{r}}{2}, \qquad \mathbf{y} = \mathbf{b} - \frac{\mathbf{r}}{2}, \tag{22}$$

as illustrated in Fig. 2. By $N_c = 3$ we denote the number of colors and $V(\mathbf{x})$ is a lightlike fundamental Wilson line at the transverse coordinate $\mathbf{x}$, defined as a path-ordered exponential

$$\begin{aligned} V(\mathbf{x}) &= \mathcal{P}_+ \exp\left[ig\int_{-\infty}^{\infty} dz^+ A_a^-(z^+,\mathbf{x})t^a\right] \\ &= \mathcal{P}_+ \exp\left[ig\int_{-\infty}^{\infty} dz^+ \int d^2\mathbf{z} G(\mathbf{x}-\mathbf{z})\rho_a(z^+,\mathbf{z})t^a\right]. \end{aligned} \tag{23}$$

It describes the eikonal multiple scattering of a color charge off a classical color field. The connection between the classical color field and the color charge densities is found by solving the classical Yang-Mills equation. These Wilson lines are the basic building blocks of observables in the CGC. To get the final result one needs to average over the color charge densities ρ that the Wilson lines depend on. The Green's function relating the color field in the Wilson line to the color charge is defined as

$$G(\mathbf{x}-\mathbf{y}) = \int \frac{d^2\mathbf{k}}{(2\pi)^2} \frac{\exp\left(i\mathbf{k}\cdot(\mathbf{x}-\mathbf{y})\right)}{\mathbf{k}^2+m^2}, \tag{24}$$

where m is an infrared regulator. The IR regulator suppresses the Coulomb-like long range tails of the color fields, so that the field of an individual point charge extends to a distance of order $\frac{1}{m}$.

Now we invoke the dilute expansion for the proton and expand the dipole cross section to the first order in the proton color-charge density, or equivalently, the field strength. Expressing the Wilson lines in terms of color charges, expanding in the dilute limit and performing the double average over the color and hot spot fluctuations then yields

$$\begin{aligned} \left\langle\!\!\left\langle \frac{d\sigma_{\mathrm{dip}}^{\mathrm{p}}}{d^2\mathbf{b}}(\mathbf{b},\mathbf{r})\right\rangle\!\!\right\rangle &= \frac{g^2(N_c^2-1)N_q}{2N_c} \\ &\times \int d^2\mathbf{z}\,\Omega\left(\mathbf{b}+\frac{\mathbf{r}}{2},\mathbf{b}-\frac{\mathbf{r}}{2},\mathbf{z},\mathbf{z}\right)F_1(\mathbf{z},\mathbf{B}), \end{aligned} \tag{25}$$

where the function $F_1(\mathbf{z},\mathbf{B}) \equiv \langle \mu^2(\mathbf{z}-\mathbf{b}_i)\rangle_{\mathrm{HS}}$ describes the average color charge density. We have also defined the shorthand notation

$$\begin{aligned} \Omega(\mathbf{x},\mathbf{y},\mathbf{z},\mathbf{v}) \equiv\ & G(\mathbf{x}-\mathbf{z})G(\mathbf{x}-\mathbf{v}) + G(\mathbf{y}-\mathbf{z})G(\mathbf{y}-\mathbf{v}) \\ & - 2G(\mathbf{x}-\mathbf{z})G(\mathbf{y}-\mathbf{v}), \end{aligned} \tag{26}$$

which is convenient as the dilute expansion of the Wilson lines always has this structure of disconnected and connected transverse coordinate parts. Specifically, this structure ensures that the dipole cross section vanishes identically in the limit $\mathbf{x} = \mathbf{y}$, where the quark and antiquark hit the target at the same transverse position. In this configuration the $Q\bar{Q}$-dipole appears color neutral and thus does not interact with the color field of the target. More details on this derivation are given in Appendix A.

Within our hot spot model the average color charge density of the proton in the transverse plane $F_1(\mathbf{z},\mathbf{B})$ has already been computed in [26] and is given by

$$\begin{aligned} F_1(\mathbf{z},\mathbf{B}) &\equiv \langle \mu^2(\mathbf{z}-\mathbf{b}_i)\rangle_{\text{Hot spot}} \\ &= \left(\frac{\frac{\mu_0^2}{2\pi r_H^2}}{1+\left(\frac{N_q-1}{N_q}\right)\frac{R^2}{r_H^2}}\right)\exp\left\{-\frac{1}{2}\frac{(\mathbf{z}-\mathbf{B})^2}{r_H^2+\left(\frac{N_q-1}{N_q}\right)R^2}\right\}. \end{aligned} \tag{27}$$

Note that while to a first approximation (in the limit $R \gg r_H, N_q \gg 1$) this is just a Gaussian whose width is given by the proton radius parameter R, the constraint of fixing the center of mass of the hot spot system gives a nontrivial dependence on the number of hot spots N_q and the hot spot radius r_H. We will call the quantity setting the scale of the impact parameter dependence in the exponential *the coherent radius*,

$$R_C^2 = r_H^2 + \left(\frac{N_q-1}{N_q}\right)R^2. \tag{28}$$

This quantity represents the effective size of the hot spot system of color charges, taking into account both the locations of the hot spots and the size of an individual hot spot.

Next, as the $\Psi_V^*\Psi_\gamma$ wave function overlap does not depend on the impact parameter ($\mathbf{b}$) of the dipole, we can compute the Fourier transform of the dipole cross sections with respect to the impact parameter

$$\begin{aligned} &\int d^2\mathbf{b} e^{-i\mathbf{b}\cdot\Delta}\left\langle\!\!\left\langle \frac{d\sigma_{\mathrm{dip}}^{\mathrm{p}}}{d^2\mathbf{b}}(\mathbf{b},\mathbf{r})\right\rangle\!\!\right\rangle \\ &= \frac{g^2\mu_0^2(N_c^2-1)N_q}{2\pi N_c}\exp\left\{-\frac{1}{2}\left(r_H^2+\left(\frac{N_q-1}{N_q}\right)R^2\right)\Delta^2\right\} \\ &\times\left\{\cos\left(\frac{1}{2}\Delta\cdot\mathbf{r}\right)\Psi(0,\Delta,m^2) - \Psi(\mathbf{r},\Delta,m^2)\right\}. \end{aligned} \tag{29}$$

which then directly enters the scattering amplitude in Eq. (1). In order to obtain Eq. (29) we have expressed the products of Green functions in Eq. (26) in momentum space, and evaluated the integrals by a Feynman parametrization. This provides the following integral representation of the function $\Psi(\mathbf{r},\Delta,m^2)$

$$\Psi(\mathbf{r},\Delta,m^2)=\int_0^{\frac{1}{2}}d\lambda\,\cos(\lambda\Delta\cdot\mathbf{r})\times\frac{|\mathbf{r}|K_1\left(|\mathbf{r}|\sqrt{-\Delta^2\lambda^2+\frac{1}{4}\Delta^2+m^2}\right)}{\sqrt{-\Delta^2\lambda^2+\frac{1}{4}\Delta^2+m^2}},\quad(30)$$

where λ is a Feynman parameter, Δ is the momentum transfer between the dipole and the proton system and m is the IR regulator. We note that the Feynman parameter integral can be evaluated exactly in the limit $\mathbf{r}\to 0$ of a zero size dipole as

$$\Psi(0,\Delta,m^2)=\int_0^{\frac{1}{2}}d\lambda\frac{1}{-\Delta^2\lambda^2+\frac{1}{4}\Delta^2+m^2}=\frac{2\mathrm{arctanh}\left(\frac{|\Delta|}{\sqrt{\Delta^2+4m^2}}\right)}{|\Delta|\sqrt{\Delta^2+4m^2}},\quad(31)$$

and it can be expanded to in powers of $\mathbf{r}$, to obtain an analytical expression of the coherent amplitude in the small dipole size limit ($m|\mathbf{r}|,|\Delta\mathbf{r}|\ll 1$). This limit is discussed in more detail in Appendix D. In Appendix D 1 we compute the cross sections at the limit of small $\mathbf{r}$, in D 2 and D 3 we discuss some analytical limits attainable at some regions of t in the small-$\mathbf{r}$ limit and in D 4 we compare the limits to the full results.

Next we will calculate the Fourier transform of the average of the square of the dipole cross section, $\langle\!\langle\frac{d\sigma^{\mathrm{p}}_{\mathrm{dip}}}{d^2\mathbf{b}}(\mathbf{b},\mathbf{r})\frac{d\sigma^{\mathrm{p}}_{\mathrm{dip}}}{d^2\bar{\mathbf{b}}}(\bar{\mathbf{b}},\bar{\mathbf{r}})\rangle\!\rangle$ which is needed for the calculation of the incoherent cross section. We will separate this contribution into four parts, based on the criteria a) whether the color structure in the amplitude and conjugate amplitude is connected (C) or disconnected (DC), and b) whether the gluon fields in the amplitude and conjugate amplitude originate from the same single (1) hot spot or two different (2) hot spots. Based on this separation the four individual parts can be evaluated as

$$\left[\int d^2\mathbf{b}d^2\bar{\mathbf{b}}e^{-i\mathbf{b}\cdot\Delta+i\bar{\mathbf{b}}\cdot\Delta}\left\langle\!\!\left\langle\frac{d\sigma^{\mathrm{p}}_{\mathrm{dip}}}{d^2\mathbf{b}}(\mathbf{b},\mathbf{r})\frac{d\sigma^{\mathrm{p}}_{\mathrm{dip}}}{d^2\bar{\mathbf{b}}}(\bar{\mathbf{b}},\bar{\mathbf{r}})\right\rangle\!\!\right\rangle\right]_{1,DC}=\frac{g^4\mu_0^4(N_c^2-1)^2N_q}{(2\pi)^2N_c^2}\exp(-r_H^2\Delta^2)\left\{\Psi(\mathbf{r})\Psi(\bar{\mathbf{r}})+\cos\left(\frac{1}{2}\Delta\cdot\mathbf{r}\right)\cos\left(\frac{1}{2}\Delta\cdot\bar{\mathbf{r}}\right)\Psi(0)\Psi(0)-\cos\left(\frac{1}{2}\Delta\cdot\bar{\mathbf{r}}\right)\Psi(\mathbf{r})\Psi(0)-\cos\left(\frac{1}{2}\Delta\cdot\mathbf{r}\right)\Psi(\bar{\mathbf{r}})\Psi(0)\right\}\quad(32)$$

$$\left[\int d^2\mathbf{b}d^2\bar{\mathbf{b}}e^{-i\mathbf{b}\cdot\Delta+i\bar{\mathbf{b}}\cdot\Delta}\left\langle\!\!\left\langle\frac{d\sigma^{\mathrm{p}}_{\mathrm{dip}}}{d^2\mathbf{b}}(\mathbf{b},\mathbf{r})\frac{d\sigma^{\mathrm{p}}_{\mathrm{dip}}}{d^2\bar{\mathbf{b}}}(\bar{\mathbf{b}},\bar{\mathbf{r}})\right\rangle\!\!\right\rangle\right]_{2,DC}=\frac{g^4\mu_0^4(N_c^2-1)^2N_q(N_q-1)}{N_c^2(2\pi)^2}\exp(-(R^2+r_H^2)\Delta^2)\left\{\Psi(\mathbf{r})\Psi(\bar{\mathbf{r}})+\cos\left(\frac{1}{2}\Delta\cdot\mathbf{r}\right)\cos\left(\frac{1}{2}\Delta\cdot\bar{\mathbf{r}}\right)\Psi(0)\Psi(0)-\cos\left(\frac{1}{2}\Delta\cdot\bar{\mathbf{r}}\right)\Psi(\mathbf{r})\Psi(0)-\cos\left(\frac{1}{2}\Delta\cdot\mathbf{r}\right)\Psi(\bar{\mathbf{r}})\Psi(0)\right\}\quad(33)$$

$$\left[\int d^2\mathbf{b}d^2\bar{\mathbf{b}}e^{-i\mathbf{b}\cdot\Delta+i\bar{\mathbf{b}}\cdot\Delta}\left\langle\!\!\left\langle\frac{d\sigma^{\mathrm{p}}_{\mathrm{dip}}}{d^2\mathbf{b}}(\mathbf{b},\mathbf{r})\frac{d\sigma^{\mathrm{p}}_{\mathrm{dip}}}{d^2\bar{\mathbf{b}}}(\bar{\mathbf{b}},\bar{\mathbf{r}})\right\rangle\!\!\right\rangle\right]_{1,C}=\frac{g^4\mu_0^4(N_c^2-1)}{64\pi^4N_c^2}N_q\int d^2\mathbf{k}d^2\bar{\mathbf{k}}\frac{\exp(-r_H^2(\mathbf{k}+\bar{\mathbf{k}})^2)}{((\mathbf{k}+\frac{\Delta}{2})^2+m^2)((\mathbf{k}-\frac{\Delta}{2})^2+m^2)}\frac{1}{((\bar{\mathbf{k}}+\frac{\Delta}{2})^2+m^2)((\bar{\mathbf{k}}-\frac{\Delta}{2})^2+m^2)}\times\left\{8\cos\left(\frac{\Delta}{2}\cdot\mathbf{r}\right)\cos\left(\frac{\Delta}{2}\cdot\bar{\mathbf{r}}\right)-8\cos\left(\frac{\Delta}{2}\cdot\mathbf{r}\right)\exp(i\bar{\mathbf{k}}\cdot\bar{\mathbf{r}})-8\cos\left(\frac{\Delta}{2}\cdot\bar{\mathbf{r}}\right)\exp(i\mathbf{k}\cdot\mathbf{r})+4\exp(i\mathbf{k}\cdot\mathbf{r}+i\bar{\mathbf{k}}\cdot\bar{\mathbf{r}})+4\exp(i\mathbf{k}\cdot\mathbf{r}-i\bar{\mathbf{k}}\cdot\bar{\mathbf{r}})\right\}\quad(34)$$

and

$$\left[\int d^2\mathbf{b}d^2\bar{\mathbf{b}}e^{-i\mathbf{b}\cdot\Delta+i\bar{\mathbf{b}}\cdot\Delta}\left\langle\!\!\left\langle\frac{d\sigma^{\mathrm{p}}_{\mathrm{dip}}}{d^2\mathbf{b}}(\mathbf{b},\mathbf{r})\frac{d\sigma^{\mathrm{p}}_{\mathrm{dip}}}{d^2\bar{\mathbf{b}}}(\bar{\mathbf{b}},\bar{\mathbf{r}})\right\rangle\!\!\right\rangle\right]_{2,C}$$
$$=\frac{g^4\mu_0^4(N_c^2-1)}{64\pi^4N_c^2}N_q(N_q-1)\int d^2\mathbf{k}d^2\bar{\mathbf{k}}\frac{\exp\left(-(R^2+r_H^2)(\mathbf{k}+\bar{\mathbf{k}})^2\right)}{((\mathbf{k}+\frac{\Delta}{2})^2+m^2)((\mathbf{k}-\frac{\Delta}{2})^2+m^2)}\frac{1}{((\bar{\mathbf{k}}+\frac{\Delta}{2})^2+m^2)((\bar{\mathbf{k}}-\frac{\Delta}{2})^2+m^2)}$$
$$\times\left\{8\cos\left(\frac{\Delta}{2}\cdot\mathbf{r}\right)\cos\left(\frac{\Delta}{2}\cdot\bar{\mathbf{r}}\right)-8\cos\left(\frac{\Delta}{2}\cdot\mathbf{r}\right)\exp\left(i\bar{\mathbf{k}}\cdot\bar{\mathbf{r}}\right)-8\cos\left(\frac{\Delta}{2}\cdot\bar{\mathbf{r}}\right)\exp\left(i\mathbf{k}\cdot\mathbf{r}\right)\right.$$
$$\left.+4\exp\left(i\mathbf{k}\cdot\mathbf{r}+i\bar{\mathbf{k}}\cdot\bar{\mathbf{r}}\right)+4\exp\left(i\mathbf{k}\cdot\mathbf{r}-i\bar{\mathbf{k}}\cdot\bar{\mathbf{r}}\right)\right\}. \tag{35}$$

While the incoherent cross section is of course only sensitive to the sum of all of these contributions, the above distinction is useful to organize the calculation and separate the effects of different sources of fluctuations. Specifically, for the contributions labeled 1 (as in "1 hot spot") the gluon fields in both the amplitude and the conjugate amplitude originate from the same hot spot, making the contribution correlated in the hot spot sense. These contributions are explicitly proportional to the number of hot spots N_q. On the other hand for the contributions labeled 2 (as in "2 hot spot"), the gluon fields originate from two different hot spots and these terms are proportional to the number of hot spot pairs $N_q(N_q-1)$. Somewhat counterintuitively these two hot spot contributions are also correlated in terms of hot spot location fluctuations, due to the fact that the center of mass of the hot spot system is fixed. A more detailed derivation of these expressions in presented in Appendix B.

Since for the color-disconnected (DC) diagrams, the CGC averages can be performed separately in the amplitude and its conjugate, the structure of the resulting expressions is similar to the coherent amplitude in Eq. (29) and again involves the same function $\Psi(\mathbf{r},\Delta,m^2)$ defined in Eq. (30). Conversely, the color-connected (C) contributions contain nontrivial color correlations between the amplitude and conjugate amplitude, which are suppressed by a relative factor $1/(N_c^2-1)$ and involve a different structure of the Green's functions. We note that in our calculation, the clear separation into color connected and disconnected parts is easily possible due to the dilute expansion and the fact that correlations of color charges are assumed to be Gaussian.

E. Cross sections

Now we will use the results obtained above for the target averages of the dipole amplitude and its square to compute the average and the square average of the vector meson scattering amplitude in Eq. (1). This will allow us to evaluate the coherent and incoherent cross sections in the hot spot model. Evaluating the square of the average, one has

$$\left|\left\langle\!\!\left\langle\mathcal{A}^{\gamma^*p\to Vp}_{T,L}(Q^2,\Delta)\right\rangle\!\!\right\rangle\right|^2=\int d^2\mathbf{r}d^2\bar{\mathbf{r}}\int d^2\mathbf{b}d^2\bar{\mathbf{b}}\int\frac{dz}{4\pi}\frac{d\bar{z}}{4\pi}(\Psi^*\Psi_V)_{T,L}(Q^2,\mathbf{r},z)(\Psi^*\Psi_V)^*_{T,L}(Q^2,\bar{\mathbf{r}},\bar{z})\exp\left\{-i\left[\mathbf{b}+\left(\frac{1}{2}-z\right)\mathbf{r}\right]\cdot\Delta\right\}$$
$$\times\exp\left\{i\left[\bar{\mathbf{b}}+\left(\frac{1}{2}-\bar{z}\right)\bar{\mathbf{r}}\right]\cdot\Delta\right\}\left\langle\!\!\left\langle\frac{d\sigma^{\mathrm{p}}_{\mathrm{dip}}}{d^2\mathbf{b}}(\mathbf{b},\mathbf{r})\right\rangle\!\!\right\rangle\left\langle\!\!\left\langle\frac{d\sigma^{\mathrm{p}}_{\mathrm{dip}}}{d^2\bar{\mathbf{b}}}(\bar{\mathbf{b}},\bar{\mathbf{r}})\right\rangle\!\!\right\rangle, \tag{36}$$

whereas the average of the square reads

$$\left\langle\!\!\left\langle|\mathcal{A}^{\gamma^*p\to Vp}_{T,L}(Q^2,\Delta)|^2\right\rangle\!\!\right\rangle=\int d^2\mathbf{r}d^2\bar{\mathbf{r}}\int d^2\mathbf{b}d^2\bar{\mathbf{b}}\int\frac{dz}{4\pi}\frac{d\bar{z}}{4\pi}(\Psi^*\Psi_V)_{T,L}(Q^2,\mathbf{r},z)(\Psi^*\Psi_V)^*_{T,L}(Q^2,\bar{\mathbf{r}},\bar{z})$$
$$\times\exp\left\{-i\left[\mathbf{b}+\left(\frac{1}{2}-z\right)\mathbf{r}\right]\cdot\Delta\right\}\exp\left\{i\left[\bar{\mathbf{b}}+\left(\frac{1}{2}-\bar{z}\right)\bar{\mathbf{r}}\right]\cdot\Delta\right\}\left\langle\!\!\left\langle\frac{d\sigma^{\mathrm{p}}_{\mathrm{dip}}}{d^2\mathbf{b}}(\mathbf{b},\mathbf{r})\frac{d\sigma^{\mathrm{p}}_{\mathrm{dip}}}{d^2\bar{\mathbf{b}}}(\bar{\mathbf{b}},\bar{\mathbf{r}})\right\rangle\!\!\right\rangle. \tag{37}$$

We first note, that in the nonrelativistic approximation, the z-integral can trivially be performed. The z-dependent piece of the scattering amplitude reads

$$\int\frac{dz}{4\pi}(\Psi_V^*\Psi_\gamma)_{T,L}e^{-i(\frac{1}{2}-z)\mathbf{r}\cdot\Delta}, \tag{38}$$

which, for the transverse and longitudinal amplitude respectively, yields

$$\int\frac{dz}{4\pi}(\Psi_V^*\Psi_\gamma)_T e^{-i(\frac{1}{2}-z)\mathbf{r}\cdot\Delta}$$
$$=-A_Q\frac{\sqrt{2m_QN_c}}{4\pi}e_Qe K_0(\varepsilon'|\mathbf{r}|)\equiv C_T K_0(\varepsilon'|\mathbf{r}|) \tag{39}$$

and

$$\int \frac{dz}{4\pi}(\Psi_V^*\Psi_\gamma)_L e^{-i(\frac{1}{2}-z)\mathbf{r}\cdot\Delta} = -A_Q\sqrt{\frac{2N_c}{m_Q}}\frac{e_Q e Q}{8\pi}K_0(\varepsilon'|\mathbf{r}|) \equiv C_L K_0(\varepsilon'|\mathbf{r}|), \quad (40)$$

where

$$\varepsilon' = \sqrt{\frac{Q^2}{4}+m_Q^2}. \quad (41)$$

We have also defined the notations

$$C_T \equiv -A_Q\frac{\sqrt{2m_Q N_c}}{4\pi}e_Q e, \quad (42)$$

$$C_L \equiv -A_Q\sqrt{\frac{2N_c}{m_Q}}\frac{e_Q e Q}{8\pi}, \quad (43)$$

for the different coefficients for the transverse and longitudinal scattering amplitudes.

Now by plugging the wave function overlap (39), (40) and the dipole cross section average (29) into the definition of the amplitude (1), we get

$$|\langle\langle\mathcal{A}_{T,L}^{\gamma^* p\to Vp}(Q^2,\Delta)\rangle\rangle|^2 = C_{T,L}^2\frac{g^4\mu_0^4(N_c^2-1)^2N_q^2}{(2\pi N_c)^2}\exp\left(-\left[r_H^2+\left(\frac{N_q-1}{N_q}\right)R^2\right]\Delta^2\right) \times\left[\int d^2\mathbf{r}K_0(\varepsilon'|\mathbf{r}|) \times\left\{\cos\left(\frac{1}{2}\Delta\cdot\mathbf{r}\right)\Psi(0,\Delta,m^2)-\Psi(\mathbf{r},\Delta,m^2)\right\}\right]^2. \quad (44)$$

Since the coherent cross section, as well as all color-disconnected contributions to the incoherent cross section give rise to the same contribution for the dipole size dependent part of the expressions, it is convenient to define the notation

$$Z(\Delta,m^2,\varepsilon') \equiv \int d^2\mathbf{r}K_0(\varepsilon'|\mathbf{r}|)\left\{\cos\left(\frac{1}{2}\Delta\cdot\mathbf{r}\right)\Psi(0,\Delta,m^2)-\Psi(\mathbf{r},\Delta,m^2)\right\}. \quad (45)$$

In terms of this function the coherent vector meson production cross section in Eq. (2) is then given by

$$\frac{d\sigma_{T,L}^{\gamma^* p\to Vp}}{dt} = \frac{C_{T,L}^2}{16\pi}\frac{g^4\mu_0^4(N_c^2-1)^2N_q^2}{(2\pi N_c)^2} \times\exp\left(-\left[r_H^2+\left(\frac{N_q-1}{N_q}\right)R^2\right]\Delta^2\right)Z(\Delta,m^2,\varepsilon')^2. \quad (46)$$

Now we can clearly see the structure of this expression. It is factorized into a constant times a Gaussian in Δ times some function Z. The width of the Gaussian depends on the parameters R and r_H characterizing the sizes of the proton and the hot spot in the combination that we call the coherent radius (28). In a naive picture these would be the only parameters determining the t-dependence of the cross section. Here, however, this t-dependence is modified by the Z-function, which depends on Coulomb tails of the color charges (through the IR regulator m), and the photon and vector meson wave functions. In the fully nonrelativistic limit the photon wave function forces the dipole size $\mathbf{r}$ to be small. In this limit one can further evaluate the Feynman parameter and dipole size ($\mathbf{r}$) integrals analytically. This limit is discussed in more detail in Appendix D.

Let us now turn to the incoherent cross section. We separate it into four distinct parts

$$\frac{d\sigma_{T,L}^{\gamma^* p\to Vp^*}}{dt} = \frac{1}{16\pi}(\langle\langle|\mathcal{A}_{T,L}^{\gamma^* p\to Vp}(Q^2,\Delta)|^2\rangle\rangle - |\langle\langle\mathcal{A}_{T,L}^{\gamma^* p\to Vp}(Q^2,\Delta)\rangle\rangle|^2) = \left.\frac{d\sigma_{T,L}^{\gamma^* p\to Vp^*}}{dt}\right|_{1,DC}+\left.\frac{d\sigma_{T,L}^{\gamma^* p\to Vp^*}}{dt}\right|_{2,DC} + \left.\frac{d\sigma_{T,L}^{\gamma^* p\to Vp^*}}{dt}\right|_{1,C}+\left.\frac{d\sigma_{T,L}^{\gamma^* p\to Vp^*}}{dt}\right|_{2,C}, \quad (47)$$

which correspond to the contributions from hot spot fluctuations with gluons coming from one (1,DC) or two (2,DC) hot spots, and the contributions due to color charge fluctuations with gluons from one (1,C) or two (2,C) hot spots. Due to its disconnected color structure, the square of the coherent amplitude is subtracted from the color disconnected contribution, and distributed proportionally in N_q between the one and two hot spot contributions. Using the function Z introduced for the coherent case in Eq. (45), the contributions due to hot spot fluctuations can then be expressed as

$$\left.\frac{d\sigma_{T,L}^{\gamma^* p\to Vp^*}}{dt}\right|_{1,DC} = \frac{C_{T,L}^2}{16\pi}\frac{g^4\mu_0^4(N_c^2-1)^2}{(2\pi N_c)^2}N_q\left[\exp(-\Delta^2 r_H^2) - \exp\left(-\left[r_H^2+\left(\frac{N_q-1}{N_q}\right)R^2\right]\Delta^2\right)\right] \times Z(\Delta,m^2,\varepsilon')^2 \quad (48)$$

and

$$\left.\frac{d\sigma_{T,L}^{\gamma^* p\to Vp^*}}{dt}\right|_{2,DC} = \frac{C_{T,L}^2}{16\pi}\frac{g^4\mu_0^4(N_c^2-1)^2}{(2\pi N_c)^2}N_q(N_q-1) \times\left[\exp\left(-\Delta^2[R^2+r_H^2]\right)-\exp\left(-\left[r_H^2+\left(\frac{N_q-1}{N_q}\right)R^2\right]\Delta^2\right)\right]Z(\Delta,m^2,\varepsilon')^2. \tag{49}$$

The contributions due to color charge fluctuations have a more complicated structure due to the two nonfactorizing color charge two-point correlators, and we were not able to find an equally simple form for them as we have for the function Z. For these contributions we are forced to leave the two transverse momentum integrals for numerical evaluation. Let use define another auxiliary notation for these integrals as

$$K(A,\Delta,m^2,\varepsilon'^2) \equiv \int d^2\mathbf{k}d^2\bar{\mathbf{k}}\frac{\exp\left(-A(\mathbf{k}+\bar{\mathbf{k}})^2\right)}{((\mathbf{k}+\frac{\Delta}{2})^2+m^2)((\mathbf{k}-\frac{\Delta}{2})^2+m^2)}\times\frac{1}{((\bar{\mathbf{k}}+\frac{\Delta}{2})^2+m^2)((\bar{\mathbf{k}}-\frac{\Delta}{2})^2+m^2)} \times\left(\frac{1}{\varepsilon'^2+\frac{\Delta^2}{4}}-\frac{1}{\varepsilon'^2+\mathbf{k}^2}\right)\left(\frac{1}{\varepsilon'^2+\frac{\Delta^2}{4}}-\frac{1}{\varepsilon'^2+\bar{\mathbf{k}}^2}\right). \tag{50}$$

Using this notation the contributions due to color charges fluctuations can be expressed in a similarly compact form as

$$\left.\frac{d\sigma_{T,L}^{\gamma^* p\to Vp^*}}{dt}\right|_{1,C} = \frac{C_{T,L}^2}{16\pi}\frac{g^4\mu_0^4(N_c^2-1)}{2\pi^2N_c^2}N_qK(r_H^2,\Delta,m^2,\varepsilon'^2) \tag{51}$$

and

$$\left.\frac{d\sigma_{T,L}^{\gamma^* p\to Vp^*}}{dt}\right|_{2,C} = \frac{C_{T,L}^2}{16\pi}\frac{g^4\mu_0^4(N_c^2-1)}{2\pi^2N_c^2}N_q(N_q-1)K(R^2+r_H^2,\Delta,m^2,\varepsilon'^2). \tag{52}$$

Before we proceed to evaluate the cross section numerically, some important comments are in order. We first note that in the limit of a single hot spot $N_q = 1$, the color disconnected (DC) contributions vanish as they should. This is due to the fact that for $N_q = 1$ the only hot spot is always at the center of mass of the proton, and thus there are no hot spot fluctuations. In this case all contributions to the incoherent cross section come from the color charge fluctuations associated with the color connected (C) contributions. We further note that at first sight the two hot spot disconnected ("2,DC") contribution might seem like an uncorrelated contribution that should not influence the incoherent cross section since it is disconnected in both color and the hot spot averaging. However, in reality it is correlated through the fixed center of mass of the hot spot system and thus contributes to the incoherent cross section.

By closer inspection of Eqs. (48) and (49) one finds that, similarly to the coherent cross section Eq. (46), the color disconnected contributions to the incoherent cross section factorize into two parts. Firstly, there are parts that are Gaussian in Δ, depending on the parameters of the hot spot system. The t-dependence is then modified by the Δ-dependence of the residual part of the cross section $Z(\Delta,m^2,\varepsilon')^2$, which also depends on the IR regulator (m) and the properties of the probe (ε'). In contrast, the color connected contributions to the incoherent cross section in Eqs. (51) and (52) do not factorize like this except for the $-t\to\infty$ limit with the small dipole size approximation that is true in the nonrelativistic quark limit. We again discuss the small dipole size approximation of these results in Appendix D.

III. ANALYSIS OF RESULTS

In this section we will study the coherent and incoherent cross sections and their dependence on the model parameters.

If not stated otherwise, we will be using the following set of default parameters, where the proton size parameter $R = \sqrt{3.3}$ GeV^{-1}, the hot spot radius $r_H = \sqrt{0.7}$ GeV^{-1}, the IR regulator $m = 0.22$ GeV, the number of hot spots $N_q = 3$ and the photon virtuality $Q^2 = 0.1$ GeV^2. The radii are the same as the ones used in [21], the IR regulator was chosen to be of the order of the QCD scale and the number of hot spots was motivated by the number of valence quarks in a proton. For the charm quark we use the mass of $m_c = 1.275$ GeV, for the bottom quark $m_b = 4.18$ GeV and for the top quark we use $m_t = 173$ GeV.

The full cross section measured experimentally in electron-proton scattering can be approximately expressed

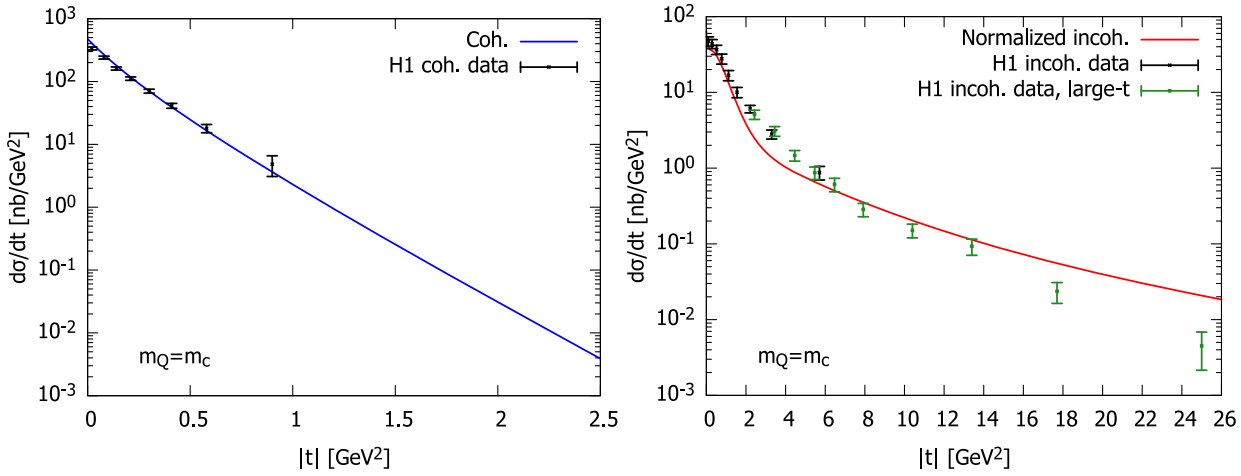

FIG. 3. Coherent and incoherent exclusive J/Ψ production cross sections compared to HERA data. The normalization of the incoherent cross section has been increased by a factor of 2.5 as explained in the text. The H1 coherent data is from [3], the lower-$|t|$ incoherent data is also from [3] and the higher-$|t|$ data is from [2]. Note that the different incoherent data sets have a slightly different Q^2 and a different center of mass energy range. Note also that the t range for the incoherent cross section data goes much further than in most works except for at least [25].

as the sum of the transverse and longitudinal cross sections as [35]

$$\sigma \approx \sigma_T + \sigma_L. \tag{53}$$

In Fig. 3 we compare the predictions of our model for the coherent and incoherent exclusive J/Ψ cross sections to HERA data. We note that our model has a free normalization parameter $g^4\mu_0^4$ which can be adjusted e.g., to the coherent cross section at low momentum transfer $|t|$. We use the value $g^4\mu_0^4 = 43.222$. Note that this parameter is dimensionless due to the way we define the profile of a hot spot in Eq. (15). However, we find that the model underpredicts the ratio of the incoherent to the coherent cross section. This clearly points to the absence of a necessary additional physical source of fluctuations, operative over a broad range in t, from our model. In order to better compare the $|t|$-dependence in spite of this mismatch, we have separately adjusted the normalization of the incoherent cross section in Fig. 3, increasing it by a factor of 2.5 relative to the coherent cross section, to better match the experimental data. While the relative normalization does not work as well as one could have hoped, by normalizing the two cross sections separately, the model seems to reproduce the general features of $|t|$-dependence of the data rather well. The normalization mismatch prevents us from performing a fit of the parameters of our model to experimental data. Instead, we will now focus on investigating further how the different features of the t-dependence emerge and how they depend on the physical parameters.

In Fig. 4 one can see plots of the cross sections with our default parameters for the three quarks masses. The figures in the top row show the c-quark, the middle row the b-quark, and the bottom row the t-quark. The left-hand side plots have a linear scale in t and the right-hand side plots a logarithmic one. We show both in order to highlight different aspects of the cross sections. The top panels of the subfigures show the total coherent and the incoherent cross sections, where—unlike in Fig. 3—the relative normalization of the coherent and incoherent cross sections is the same. However we have scaled the cross sections with the ratio of the decay widths, and by the quark masses to the fifth power. This scaling cancels out the leading quark mass dependence in the fully nonrelativistic limit, which corresponds to the small dipole size approximation discussed in Appendix D. This limit can also be seen, up to a logarithmic dependence on the mass, from the coherent cross section at $t = 0$ without an expansion in $\mathbf{r}$, as shown in Appendix C. Scaling with the decay width also fully cancels out the dependence on the wave function normalization constant A_q [see Eq. (10)] so that we do not need to pick any specific value for A_q.

The total incoherent cross section is further separated into its color and hot spot fluctuation contributions. These can be seen in the top panels as well. The bottom panels show the relative contributions of all four different parts of the incoherent cross section to the full incoherent cross section. The two hot spot color disconnected contribution becomes negative due to the way we subtract the coherent cross section proportionally in N_q. However the sum of all contributions is always equal to unity, which is why the one hot spot color disconnected contribution can be larger than the total incoherent cross section.

We have also added lines to Fig. 4 representing the behavior of the cross sections that could be expected from a nonrelativistic heavy quark limit in specific ranges in t. The normalization of these lines is adjusted by hand for better

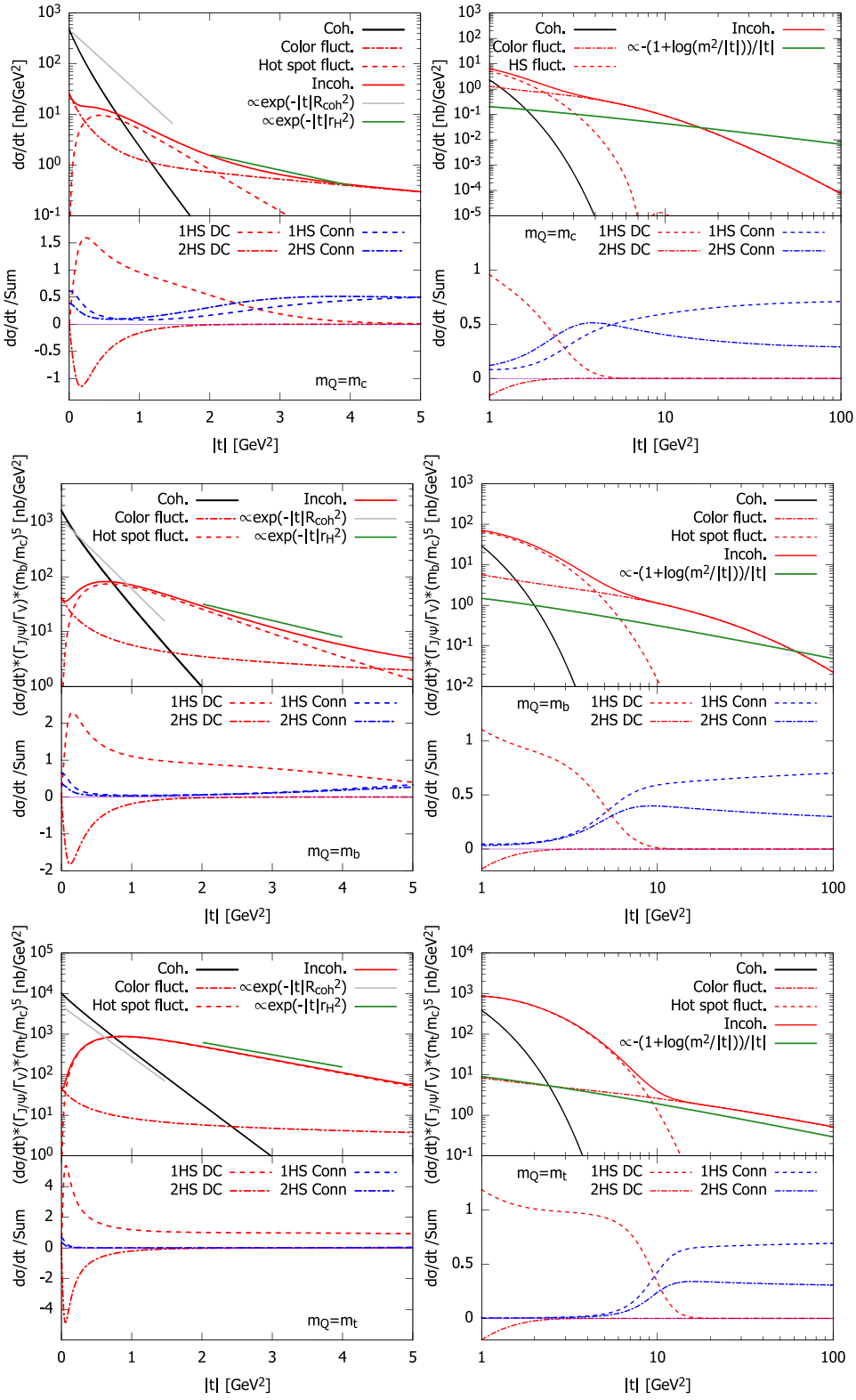

FIG. 4. Coherent and incoherent cross sections as a function of t for $c\bar{c}$ (top panel), $b\bar{b}$ (middle panel) and $t\bar{t}$ (bottom panel). Cross sections for the $b\bar{b}$ and $t\bar{t}$ mesons V are scaled as $(d\sigma/dt)(\Gamma_{J/\Psi}/\Gamma_V)(m_Q/m_c)^5$ to absorb the leading quark mass dependence. We also show a breakup of the incoherent cross section into different contributions. The top plots in each subfigure show the coherent cross section and the incoherent cross section with an additional separation of the incoherent cross section into hot spot and color fluctuation contributions. The bottom plots of the subfigures show the relative contribution of each part of the incoherent cross section to the total incoherent cross section. Also shown is the expected behavior of the cross sections in specific ranges of $|t|$, as discussed in the text.

visibility. Plots using the actual normalization constants of the limits are shown in Fig. 7 in Appendix D. The nonrelativistic expectations shown in the figure are the following ones:

(i) By looking at the coherent cross section Eq. (46), one would be tempted to neglect the dependence of the function Z on Δ. Thus, to a first approximation the coherent cross section at small t is expected to behave as

$$\frac{d\sigma_{T,L}^{\gamma^* p\to Vp}}{dt} \propto \exp(R_C^2 t), \tag{54}$$

with the coherent radius given by Eq. (28). This behavior, however, receives corrections from the long range Coulomb tails regulated by m. These corrections to the slope, as discussed in Appendix D 2, are only extremely slowly suppressed in the nonrelativistic limit, as $\sim 1/\ln m_Q$.

(ii) Similarly, the hot spot fluctuation part is expected to dominate the cross section in the range $-t \sim 1/r_H^2 \gg 1/R_C^2$ where one is probing distance scales of the hot spot radius, but not yet the very smallest scale color charge fluctuations. Here the first term of Eq. (48) dominates and one may expect

$$\frac{d\sigma_{T,L}^{\gamma^* p\to Vp^*}}{dt} \propto \exp(r_H^2 t). \tag{55}$$

(iii) Ultimately, at very large t color charge fluctuations dominate the incoherent cross section. In this region the expectation in the non-relativistic limit takes the form

$$\frac{d\sigma_{T,L}^{\gamma^* p\to Vp^*}}{dt} \propto \frac{1+\ln\frac{m^2}{-t}}{t}, \tag{56}$$

resulting from the power-law Coulomb tails of the color fields around the color charges, regulated by m as discussed in more detail in Appendix D 3 [see Eq. (D18)].

Now let us discuss what we see in the plots of Fig. 4. The coherent cross section is much larger than the incoherent cross section at small values of t. This is due to coherent cross section measuring averages of the system which are smoother as functions of the transverse position $\mathbf{b}$ that is the Fourier conjugate to $\Delta = \sqrt{-t}$. The incoherent cross section on the other hand measures fluctuations of the system and is therefore a mix of exponentially decaying hot spot fluctuation parts and color fluctuation parts that decay approximately like a power law in t. This is also why the incoherent cross section is dominated by color fluctuations at both very small and large t. The influence of the different contributions to the incoherent cross section as a function of t can best be seen in the bottom panels. Here we clearly see that, at intermediate values of t the hot spot fluctuations dominate. Then the color fluctuation contributions start to take over at large t, where one starts to resolve the color charge fluctuations inside the target (see also discussion in Refs. [44,45]).

Finally let us discuss what changes as we change the mass of the heavy quark. Let us start from our nonrelativistic limit of the top quark. Here our dipole is truly small due the large $\varepsilon' \sim m_Q$ in the photon wave function. We see that in this case the analytic expectations in the nonrelativistic limit are well satisfied, apart from the change in slope at small t caused by the Coulomb tails [see discussion in Appendix D 2, Eq. (D12)]. This is due to the fact that a large quark mass renders the Z-function almost independent of t. However, when we study the phenomenologically relevant cases of the bottom and the charm quark, we see that this is not the case. Especially the large t tail of the incoherent cross section $(-[1+\log(m^2/-t)]/-t)$ does not describe the cross section for the charm and the bottom at all, which means that the large-t and small-$\mathbf{r}$ approximation is not valid for realistic quark masses. Similarly, the exponential behavior of the coherent and incoherent cross section at small to moderate t is not entirely determined by the properties of the target. Instead, the Z-function that describes the interaction of the target with a color dipole dominates the t-dependence. Due to this discrepancy, the slope of the coherent cross section does not have a clear interpretation as a measure of the overall size of the proton as one might expect. This is one of the main results of this paper. The cross sections for realistic quark masses do not only measure the target but some more involved convolution of the target and probe structures.

Now let us move to the plots in Fig. 5. Here we vary our model parameters m, r_H and N_q that describe the hot spot structure of the proton to see how the cross sections depend on them. In all cases, the plots are made so that the coherent radius R_C defined in Eq. (28) is kept constant. Thus, when we vary the hot spot radius r_H, the proton size parameter R is changed to compensate. Similarly, when we vary the number of hot spots N_q, we keep the hot spot radius r_H fixed and vary the proton size parameter R to keep R_C fixed. With a constant coherent radius R_C the only parameter affecting the t-slope of the coherent cross section is the IR regulator m, which affects the t-distribution via the Z-function. We also normalize all cases to have the same amount of color charge, which in practice means that we add a normalizing factor of $\frac{3}{N_q}$ in front of the sum over the hot spots in the color charge density two point correlator in Eq. (14). This ensures that the proton always has the same overall amount of color charges as in the case of $N_q = 3$. We thus remove the trivial effect of the N_q variation on the normalization of the cross section. We do not plot separately a variation of the proton size parameter R, since this case would either result in a variation of the coherent radius

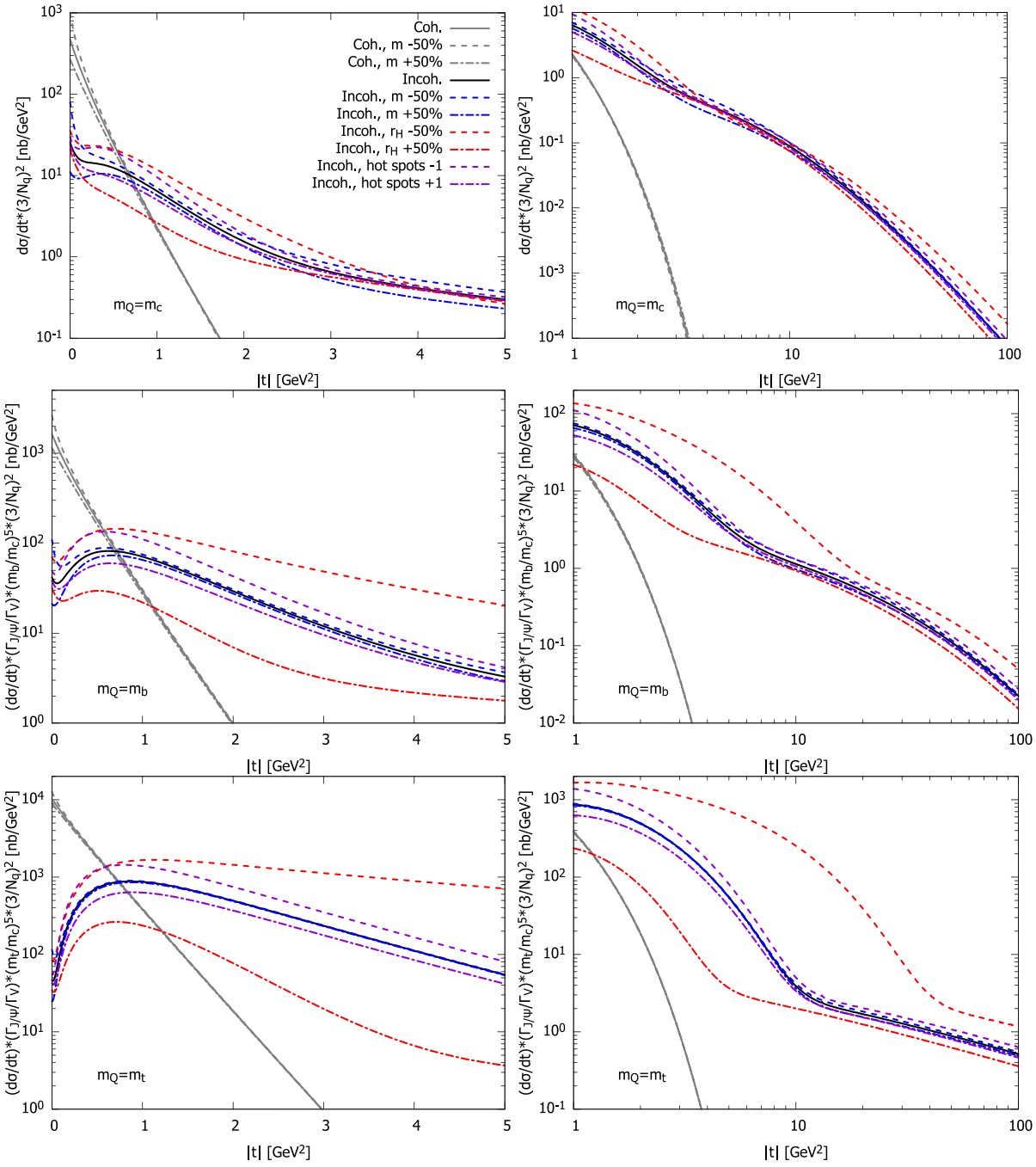

FIG. 5. Effect of variations of the model parameters m, r_H and N_q on the t-dependence of the coherent and incoherent cross sections for $c\bar{c}$ (top panel), $b\bar{b}$ (middle panel) and $t\bar{t}$ (bottom panel). Cross sections are scaled as $(d\sigma/dt)(\Gamma_{J/\Psi}/\Gamma_V)(m_Q/m_c)^5(3/N_q)^2$ to absorb the leading m_Q and N_q dependence. The legend in the top-left plot is valid for all the other plots. The parameter variations are made in such a way that the coherent radius R_C is kept fixed, as discussed in the text.

R_C, or when keeping R_C fixed is already included in the other cases.

We see that the larger the quark mass is, the smaller the effect of varying the IR regulator m has on the cross sections. This can be understood by noting that a large quark mass forces the dipoles to be small. In terms of equations, we can see that taking the small-r limit and expand at large $-t/m^2$ (i.e., small m), the Z-function goes as $\log(\varepsilon'/t)$ with corrections of $O(m^2)$ [see Eq. (D10) in Appendix D 2]. Thus, for small dipoles, the cross section becomes independent of m in the limit $-t \gg m^2$. For the c and b quarks, however, the IR regulator m has a significant effect on the coherent cross section at small t. Overall in the hot spot picture it is not very straightforward to

interpret the t-dependence of the coherent cross section in terms of the spatial distribution of color charges, because one is very sensitive to the Coulomb tail of the field around them. On the other hand, the t-dependence of the incoherent cross section is, perhaps surprisingly, not very sensitive to the IR cutoff m apart from the behavior at very small values of t.

Varying the hot spot radius, in the charm quark case, does not really change the slope of the medium-$|t|$ incoherent cross section. This is due to the dominance of the Z-function in this region as discussed before. The hot spot radius does, however, have an effect on the normalization. But when looking at the heavier quarks, we can see that eventually one recovers the nonrelativistic expectation, where the slope changes with a changing r_H. This effect is especially noticeable for the top quark case.

Now let us discuss the variation of N_q. By normalizing the amount of color charge in the proton with the normalization factor $(3/N_q)^2$ and by changing the proton size parameter R to keep the coherent radius R_C fixed, we keep the coherent cross section unchanged when varying N_q. For the incoherent cross section a variation in N_q most importantly means a change in the N_q weighting between the one and two hot spot contributions. After the normalization by $(3/N_q)^2$, the coefficient of the one hot spot contributions (48), (51) goes as $\propto 1/N_q$ and the coefficient of the two hot spot contributions (49), (52) as $\propto (N_q-1)/N_q$. Thus as N_q increases, the one hot spot contributions go down and the two hot spot contributions go up. However, as we see in Fig. 4 for $N_q = 3$, the one hot spot contribution is dominant at all values of t. Correspondingly, the incoherent cross section always increases with decreasing N_q and vice versa. The increase is not fully uniform in t, however, because of the varying secondary effect from the two hot spot contributions, which have a different N_q scaling.

In Fig. 6 we combine cross sections with different quark masses in the same plot, in order to better visualize the quark mass dependence. As we know, the larger the quark mass, the smaller the dipole tends to be due to the larger $\epsilon' \sim m_Q$ in the photon wave function. We again see that the larger the mass of the quark, the better the expected behaviors of the cross sections work. The cross sections have been scaled by the meson leptonic decay width and m_Q^5. This cancels the expected power law quark mass dependence, as discussed in Appendixes C and D, but leaves a logarithmic one in the coherent cross section [see Eq. (C3)] and the hot spot fluctuation part of the incoherent cross section [see Eq. (D2)]. In the numerical evaluation we see that e.g., the normalization of the charm and bottom cross sections differ from the power law by roughly an order of magnitude, so the deviations from the expected power law dependence because of these logarithms are quite substantial.

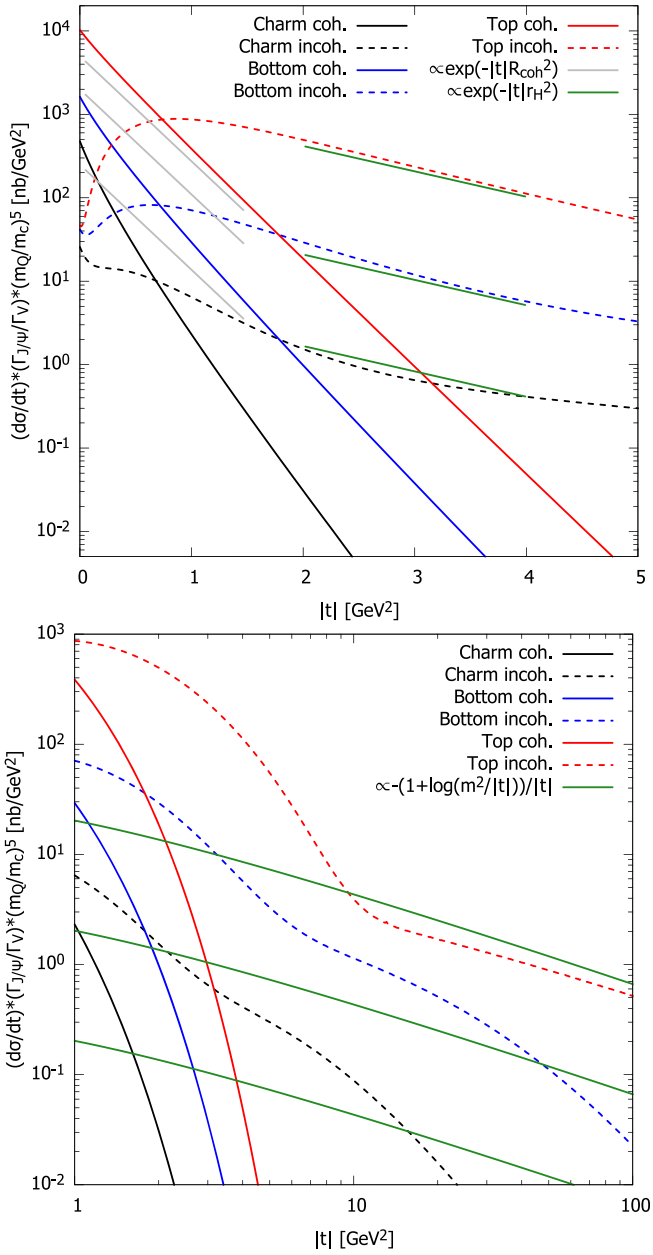

FIG. 6. Quark mass dependence of the cross section $(d\sigma/dt)(\Gamma_{J/\Psi}/\Gamma_V)(m_Q/m_c)^5$. Numerical results for $c\bar{c}$, $b\bar{b}$ and $t\bar{t}$ vector meson production are compared to the expected behavior of the cross sections in the relevant t-ranges.

IV. CONCLUSIONS

In our previous work [26] we took commonly used physics ingredients used to describe collisions involving hadrons and built an analytical model for the hot spot structure of the color field of a high energy nucleon. In this paper we have computed coherent and incoherent exclusive vector meson cross sections in this model, in order to study how such measurements can be used to understand the subnucleon scale geometry. Our emphasis has been on keeping the model simple and analytically tractable, for

instance by using the dilute expansion of the proton. This has allowed us to perform averages over both color and hot spot degrees of freedom in an analytical fashion.

Using parameter values which we think are in an acceptable, physically relevant range, we have found a clear separation into contributions sensitive to different types of fluctuations for the incoherent cross section. The hot spot fluctuations parts vanish at zero momentum transfer ($t = 0$) but become the dominant contribution quickly as t increases. After this, as t increases and the probe starts resolving the color fluctuations in the target, the color fluctuation contributions become dominant. We found that the hot spot fluctuation parts, as well as the coherent cross section, depend on the geometrical parameters of the hot spot system through an exponential in t, modified by logarithms, whereas the color fluctuation contributions decrease as power law in t, up to logarithmic corrections.

Our analytically tractable approach allowed us to gain several important insights into the relation of the hot spot structure of the nucleon and the exclusive vector meson production cross section. Firstly, in our model the normalization between the coherent and incoherent cross sections did not match experimental observations at HERA; however, the form of the t-distribution does look mostly correct as seen in Fig. 3, pointing to the presence of additional fluctuations not included in the model. Secondly we found that any realistic quark mass (c, b) results in a t-dependence of the cross section, which is sensitive to both the structure of the target and the probe, and not only the target. Thirdly we found that we can not use the small dipole size approximation in this model when studying J/Ψ production, and not even in the case of Υ when studying the incoherent cross section.

Generally, the sensitivity of the t-dependence of the cross section on the meson wave function, or the wave function overlap, dependence seems to be larger than anticipated. Usually one assumes that already for the J/Ψ the charm quarks form a dipole probe that can be treated as small. However in our model it seems that with charm, or even bottom quarks, we are still sensitive to the structure of the probe. Thus the usual intuition that the slope of the coherent cross section measures the overall size of the proton breaks down. This can also be seen when we expand the cross sections in the small dipole size approximation, which yields a drastically different asymptotic behavior of the cross sections for realistically heavy quark masses. By studying different quark masses we have seen that for heavier quarks the t-distribution does eventually become less dependent on the probe. We therefore conclude, that in order to disentangle projectile and target properties from exclusive vector meson production, it will be interesting and important to simultaneously study charmonium and bottomonium production in future experimental measurements.

Due to the discrepancy in the relative normalization of the coherent and incoherent cross section, between the experimental data and our microscopic model, we did not perform an actual fit to experimental data. We instead considered values of the model parameters that are, in our estimation, physically relevant and that have been used in previous applications to both exclusive vector meson and proton-nucleus collisions.

There are studies, using similar versions of the hot spot model, where the normalization of the cross sections works significantly better [21,28], but at this stage we can only speculate on the reasons for this discrepancy. In a Monte Carlo implementation one can define the center of mass for the gluon field, whereas we fix the center of mass of the proton to be the center of the hot spot system of color charges, but this we expect to have a negligible effect. One thing that is clearly different is the dilute expansion, which actually removes the gluon saturation aspect of our model. This might, and probably does, reduce the magnitude of gluon field fluctuations in the proton and could contribute to the normalization discrepancy, although not obviously in the correct direction. In addition to the sources of fluctuation included here, many models include additional saturation scale (Q_s) fluctuations, letting the amount of color charge change in individual hot spots fluctuate on an event-by-event basis. Such additional fluctuations clearly do increase the incoherent cross section across the t-spectrum [20]. One simplification used here is also the treatment of the wave function overlap, for which we used the nonrelativistic wave functions to keep our model simple and analytically tractable. In this limit the quark and the anti-quark in the dipole always carry half of the photon momentum ($z = 1/2$), which decouples the dipole size $\mathbf{r}$ from the transverse momentum transfer Δ. This can actually make the t-distribution at large t behave differently, as such a coupling would effectively make the typical dipoles smaller at large momentum transfer.

Clearly, as a possible future direction, it would be interesting to study how exactly the aforementioned differences to Monte Carlo implementations affect the cross sections we found here. One could e.g., try use a more general wave function with an actual dipole momentum fraction (z) dependence and see how, in general, the change of the wave function affects the results. This would be interesting because we found a large wave function dependence on the cross sections. One could also try to incorporate the Q_s fluctuations or saturation to our simple model, but it is not obvious how to do this maintaining the analytical treatment of the fluctuations. One could also include N_q fluctuations which should not be very difficult to do in our model. Finally, one additional possibility for further work could be to try and fit the microscopic hot spot model to experimental data, with or without separate normalizations for the coherent and incoherent cross sections.

ACKNOWLEDGMENTS

S. D. acknowledges the support of the Vilho, Yrjö and Kalle Väisälä Foundation. S. S. acknowledges support by the Deutsche Forschungsgemeinschaft (DFG, German Research Foundation) through the CRC-TR 211 'Strong-interaction matter under extreme conditions'- Project No. 315477589—TRR 211. S. D. and T. L. have been supported by the Academy of Finland, by the Centre of Excellence in Quark Matter (Project No. 346324) and Project No. 321840. This work has also been supported under the European Union's Horizon 2020 research and innovation programme by the STRONG-2020 project (Grant Agreement No. 824093) and by the European Research Council, Grant Agreements No. ERC-2015-CoG-681707 and No. ERC-2018-AdG-835105. The content of this article does not reflect the official opinion of the European Union and responsibility for the information and views expressed therein lies entirely with the authors.

APPENDIX A: AVERAGE OF THE DIPOLE CROSS SECTION

We start from the definition of the dipole scattering amplitude written with respect to the Wilson line dipole as

$$\frac{d\sigma^{\mathrm{p}}_{\mathrm{dip}}}{d^2\mathbf{b}}(\mathbf{b},\mathbf{r}) = 2\left(1-\frac{1}{N_c}\mathrm{Tr}[V(\mathbf{x})V^{\dagger}(\mathbf{y})]\right), \tag{A1}$$

where the Wilson lines V are the path ordered exponentials of the color field (23). We work in the dilute limit of the proton and we proceed to expand the Wilson lines to the lowest order in the proton color charge density or equivalently the proton saturation scale. This yields

$$\frac{d\sigma^{\mathrm{p}}_{\mathrm{dip}}}{d^2\mathbf{b}}(\mathbf{b},\mathbf{r}) \approx -\frac{2g^2}{N_c}\left(\mathrm{Tr}\left[\int d^2\mathbf{z}d^2\mathbf{w}G(\mathbf{x}-\mathbf{z})G(\mathbf{y}-\mathbf{w})\rho_a(\mathbf{z})\rho_b(\mathbf{w})t^a t^b\right]\right.$$
$$\left.-\frac{1}{2}\mathrm{Tr}\left[\int d^2\mathbf{z}d^2\mathbf{w}G(\mathbf{x}-\mathbf{z})G(\mathbf{x}-\mathbf{w})\rho_a(\mathbf{z})\rho_b(\mathbf{w})t^a t^b\right]-\frac{1}{2}\mathrm{Tr}\left[\int d^2\mathbf{z}d^2\mathbf{w}G(\mathbf{y}-\mathbf{z})G(\mathbf{y}-\mathbf{w})\rho_a(\mathbf{z})\rho_b(\mathbf{w})t^a t^b\right]\right), \tag{A2}$$

where G is the Green's function

$$G(\mathbf{x}-\mathbf{y}) = \int \frac{d^2\mathbf{k}}{(2\pi)^2}\frac{\exp(i\mathbf{k}\cdot(\mathbf{x}-\mathbf{y}))}{\mathbf{k}^2+m^2}. \tag{A3}$$

Next we take the trace over the $SU(N_c)$ generators and take the Gaussian averages over the color charge configurations with an MV-model color charge two point function with the added hot spot model distribution of color charges as defined in

$$\langle\rho_a(\mathbf{x})\rho_b(\mathbf{y})\rangle_{\mathrm{CGC}} = \sum_{i=1}^{N_q}\mu^2\left(\frac{\mathbf{x}-\mathbf{y}}{2}-\mathbf{b}_i\right)\delta^{(2)}(\mathbf{x}-\mathbf{y})\delta^{ab}, \tag{A4}$$

where b_i are the coordinates for the centers of the hot spots in the proton.

Now by taking the trace and the color charge average, and integrating over the transverse coordinate delta function, the dipole cross section takes the form

$$\left\langle\frac{d\sigma^{\mathrm{p}}_{\mathrm{dip}}}{d^2\mathbf{b}}(\mathbf{b},\mathbf{r})\right\rangle_{\mathrm{CGC}} \approx \frac{g^2(N_c^2-1)}{2N_c}\int d^2\mathbf{z}[G(\mathbf{x}-\mathbf{z})G(\mathbf{x}-\mathbf{z})+G(\mathbf{y}-\mathbf{z})G(\mathbf{y}-\mathbf{z})-2G(\mathbf{x}-\mathbf{z})G(\mathbf{y}-\mathbf{z})]\sum_{i=1}^{N_q}\mu^2(\mathbf{z}-\mathbf{b}_i). \tag{A5}$$

By taking the hot spot average, we get

$$\left\langle\!\left\langle\frac{d\sigma^{\mathrm{p}}_{\mathrm{dip}}}{d^2\mathbf{b}}(\mathbf{b},\mathbf{r})\right\rangle\!\right\rangle \approx \frac{g^2(N^2-1)N_q}{2N}\int d^2\mathbf{z}[G(\mathbf{x}-\mathbf{z})G(\mathbf{x}-\mathbf{z})+G(\mathbf{y}-\mathbf{z})G(\mathbf{y}-\mathbf{z})-2G(\mathbf{x}-\mathbf{z})G(\mathbf{y}-\mathbf{z})]F_1(\mathbf{z},\mathbf{B})), \tag{A6}$$

where F_1 is the same function as defined before in Eq. (27). This can be written more compactly by defining

$$\Omega(\mathbf{x},\mathbf{y},\mathbf{z},\mathbf{v}) = G(\mathbf{x}-\mathbf{z})G(\mathbf{x}-\mathbf{v})+G(\mathbf{y}-\mathbf{z})G(\mathbf{y}-\mathbf{v})-2G(\mathbf{x}-\mathbf{z})G(\mathbf{y}-\mathbf{v}), \tag{A7}$$

and writing

$$\left\langle\!\!\left\langle \frac{d\sigma^{\mathrm{p}}_{\mathrm{dip}}}{d^2\mathbf{b}}(\mathbf{b},\mathbf{r}) \right\rangle\!\!\right\rangle \approx \frac{g^2(N_c^2-1)N_q}{2N_c}\int d^2\mathbf{z}\Omega(\mathbf{x},\mathbf{y},\mathbf{z},\mathbf{z})F_1(\mathbf{z},\mathbf{B}), \tag{A8}$$

which can be written as

$$\left\langle\!\!\left\langle \frac{d\sigma^{\mathrm{p}}_{\mathrm{dip}}}{d^2\mathbf{b}}(\mathbf{b},\mathbf{r}) \right\rangle\!\!\right\rangle = \frac{g^2(N_c^2-1)N_q}{2N_c}\int d^2\mathbf{z}\Omega\left(\mathbf{b}+\frac{\mathbf{r}}{2},\mathbf{b}-\frac{\mathbf{r}}{2},\mathbf{z},\mathbf{z}\right)F_1(\mathbf{z},\mathbf{B}). \tag{A9}$$

APPENDIX B: AVERAGE OF THE DIPOLE CROSS SECTION SQUARED

Now we start from the definition of the dipole cross section squared. It is easy get from the definition of the cross section and it reads

$$\frac{d\sigma^{\mathrm{p}}_{\mathrm{dip}}}{d^2\mathbf{b}}(\mathbf{b},\mathbf{r})\frac{d\sigma^{\mathrm{p}}_{\mathrm{dip}}}{d^2\bar{\mathbf{b}}}(\bar{\mathbf{b}},\bar{\mathbf{r}}) = 2\left(1-\frac{1}{N_c}\mathrm{Tr}[V(\mathbf{x})V^\dagger(\mathbf{y})]\right)2\left(1-\frac{1}{N_c}\mathrm{Tr}[V(\bar{\mathbf{x}})V^\dagger(\bar{\mathbf{y}})]\right). \tag{B1}$$

We again expand the Wilson lines to the lowest nontrivial order in the proton color charge. After this, we take the contractions of the color charges as we did before. Now when we take hot spot averages, we take averages of two hot spots instead of just one. Thus we get a term proportional to N_q, which corresponds to measuring two gluons originating from the same hot spot, and then we have a term proportional to $N_q(N_q-1)$ that corresponds to measuring the gluons from different hot spots. After taking both of these averages, we get

$$\left\langle\!\!\left\langle \frac{d\sigma^{\mathrm{p}}_{\mathrm{dip}}}{d^2\mathbf{b}}(\mathbf{b},\mathbf{r})\frac{d\sigma^{\mathrm{p}}_{\mathrm{dip}}}{d^2\bar{\mathbf{b}}}(\bar{\mathbf{b}},\bar{\mathbf{r}}) \right\rangle\!\!\right\rangle = \frac{g^4}{4N_c^2}\int d^2\mathbf{z}d^2\mathbf{v}\{(N_c^2-1)^2\Omega(\mathbf{x},\mathbf{y},\mathbf{z},\mathbf{z})\Omega(\bar{\mathbf{x}},\bar{\mathbf{y}},\mathbf{v},\mathbf{v}) + (N_c^2-1)\Omega(\mathbf{x},\mathbf{y},\mathbf{z},\mathbf{v})\Omega(\bar{\mathbf{x}},\bar{\mathbf{y}},\mathbf{z},\mathbf{v}) + (N_c^2-1)\Omega(\mathbf{x},\mathbf{y},\mathbf{z},\mathbf{v})\Omega(\bar{\mathbf{x}},\bar{\mathbf{y}},\mathbf{v},\mathbf{z})\}\{N_qF_2(\mathbf{z},\mathbf{v},\mathbf{B}) + N_q(N_q-1)F_3(\mathbf{z},\mathbf{v},\mathbf{B})\}, \tag{B2}$$

which can be written, in the impact parameter and dipole size coordinates, as

$$\begin{aligned}\left\langle\!\!\left\langle \frac{d\sigma^{\mathrm{p}}_{\mathrm{dip}}}{d^2\mathbf{b}}(\mathbf{b},\mathbf{r})\frac{d\sigma^{\mathrm{p}}_{\mathrm{dip}}}{d^2\bar{\mathbf{b}}}(\bar{\mathbf{b}},\bar{\mathbf{r}}) \right\rangle\!\!\right\rangle = \frac{g^4}{4N_c^2}\int d^2\mathbf{z}d^2\mathbf{v}\Bigg\{&(N_c^2-1)^2\Omega\left(\mathbf{b}+\frac{\mathbf{r}}{2},\mathbf{b}-\frac{\mathbf{r}}{2},\mathbf{z},\mathbf{z}\right)\Omega\left(\bar{\mathbf{b}}+\frac{\bar{\mathbf{r}}}{2},\bar{\mathbf{b}}-\frac{\bar{\mathbf{r}}}{2},\mathbf{v},\mathbf{v}\right)\\ &+(N_c^2-1)\Omega\left(\mathbf{b}+\frac{\mathbf{r}}{2},\mathbf{b}-\frac{\mathbf{r}}{2},\mathbf{z},\mathbf{v}\right)\Omega\left(\bar{\mathbf{b}}+\frac{\bar{\mathbf{r}}}{2},\bar{\mathbf{b}}-\frac{\bar{\mathbf{r}}}{2},\mathbf{z},\mathbf{v}\right)\\ &+(N_c^2-1)\Omega\left(\mathbf{b}+\frac{\mathbf{r}}{2},\mathbf{b}-\frac{\mathbf{r}}{2},\mathbf{z},\mathbf{v}\right)\Omega\left(\bar{\mathbf{b}}+\frac{\bar{\mathbf{r}}}{2},\bar{\mathbf{b}}-\frac{\bar{\mathbf{r}}}{2},\mathbf{v},\mathbf{z}\right)\Bigg\}\\ &\times\{N_qF_2(\mathbf{z},\mathbf{v},\mathbf{B}) + N_q(N_q-1)F_3(\mathbf{z},\mathbf{v},\mathbf{B})\}.\end{aligned} \tag{B3}$$

Here we have defined

$$\begin{aligned}F_2(\mathbf{z},\mathbf{v},\mathbf{B}) &\equiv \langle\mu^2(\mathbf{z}-\mathbf{b}_i)\mu^2(\mathbf{v}-\mathbf{b}_i)\rangle_{\text{Hot spot}}\\ &= \left(\frac{\mu_0^2}{2\pi r_H^2}\right)^2\left(\frac{1}{1+2(\frac{N_q-1}{N_q})\frac{R^2}{r_H^2}}\right)\exp\left\{-\frac{(\mathbf{z}+\mathbf{v}-2\mathbf{B})^2}{4r_H^2(1+2(\frac{N_q-1}{N_q})\frac{R^2}{r_H^2})}-\frac{(\mathbf{z}-\mathbf{v})^2}{4r_H^2}\right\}\end{aligned} \tag{B4}$$

and

$$\begin{aligned}F_3(\mathbf{z},\mathbf{v},\mathbf{B}) &\equiv \langle\mu^2(\mathbf{z}-\mathbf{b}_i)\mu^2(\mathbf{v}-\mathbf{b}_j)\rangle_{\text{Hot spot}}\\ &= \left(\frac{\mu_0^4}{(2\pi)^2(R^2+r_H^2)}\right)\left(\frac{1}{r_H^2+(\frac{N_q-2}{N_q})R^2}\right)\exp\left\{-\frac{(\mathbf{z}+\mathbf{v}-2\mathbf{B})^2}{4(r_H^2+(\frac{N_q-2}{N_q})R^2)}-\frac{(\mathbf{z}-\mathbf{v})^2}{4(R^2+r_H^2)}\right\},\end{aligned} \tag{B5}$$

which we first computed in [26].

The integrals in the first term, the term proportional to $(N_c^2-1)^2$, decouple and the result is proportional to the coherent amplitude squared. The second two terms however are different. For the Fourier transform of the latter terms we use the identity

$$\begin{aligned}
&\int d^2\mathbf{b}d^2\bar{\mathbf{b}}d^2\mathbf{v}d^2\mathbf{w}e^{-i\mathbf{b}\cdot\Delta+i\bar{\mathbf{b}}\cdot\Delta}G(\mathbf{b}+\mathbf{R}_1-\mathbf{v})G(\mathbf{b}+\mathbf{R}_2-\mathbf{w})G(\bar{\mathbf{b}}+\bar{\mathbf{R}}_1-\mathbf{v})G(\bar{\mathbf{b}}+\bar{\mathbf{R}}_2-\mathbf{w})e^{-B(\mathbf{v}+\mathbf{w})^2-C(\mathbf{v}-\mathbf{w})^2}\\
&=\frac{1}{16(2\pi)^2}\frac{1}{BC}\int d^2\mathbf{k}d^2\bar{\mathbf{k}}\exp\left\{-\frac{1}{4C}(\mathbf{k}+\bar{\mathbf{k}})^2+i\mathbf{k}\cdot(\mathbf{R}_2-\mathbf{R}_1)+i\bar{\mathbf{k}}\cdot(\bar{\mathbf{R}}_2-\bar{\mathbf{R}}_1)+\frac{i\Delta}{2}\cdot(\mathbf{R}_1+\mathbf{R}_2-\bar{\mathbf{R}}_1-\bar{\mathbf{R}}_2)\right\}\\
&\quad\times\frac{1}{((\mathbf{k}+\frac{\Delta}{2})^2+m^2)((\mathbf{k}-\frac{\Delta}{2})^2+m^2)}\frac{1}{((\bar{\mathbf{k}}+\frac{\Delta}{2})^2+m^2)((\bar{\mathbf{k}}-\frac{\Delta}{2})^2+m^2)}.
\end{aligned}\tag{B6}$$

Here B and C are the coefficients of the exponentials (B4) or (B5) depending on which term we are calculating.

Now focusing on the latter two terms of (B3), using the identity (B6) and simplifying, we may write

$$\begin{aligned}
&\int d^2\mathbf{b}d^2\bar{\mathbf{b}}e^{-i\mathbf{b}\cdot\Delta+i\bar{\mathbf{b}}\cdot\Delta}\int d^2\mathbf{z}d^2\mathbf{v}\exp\{-B(\mathbf{z}+\mathbf{v})^2-C(\mathbf{z}-\mathbf{v})^2\}\left\{\Omega\left(\mathbf{b}+\frac{\mathbf{r}}{2},\mathbf{b}-\frac{\mathbf{r}}{2},\mathbf{z},\mathbf{v}\right)\Omega\left(\bar{\mathbf{b}}+\frac{\bar{\mathbf{r}}}{2},\bar{\mathbf{b}}-\frac{\bar{\mathbf{r}}}{2},\mathbf{z},\mathbf{v}\right)\right.\\
&\left.+\Omega\left(\mathbf{b}+\frac{\mathbf{r}}{2},\mathbf{b}-\frac{\mathbf{r}}{2},\mathbf{z},\mathbf{v}\right)\Omega\left(\bar{\mathbf{b}}+\frac{\bar{\mathbf{r}}}{2},\bar{\mathbf{b}}-\frac{\bar{\mathbf{r}}}{2},\mathbf{v},\mathbf{z}\right)\right\}\\
&=\frac{1}{16(2\pi)^2BC}\int d^2\mathbf{k}d^2\bar{\mathbf{k}}\frac{\exp\{-\frac{1}{4C}(\mathbf{k}+\bar{\mathbf{k}})^2\}}{((\mathbf{k}+\frac{\Delta}{2})^2+m^2)((\mathbf{k}-\frac{\Delta}{2})^2+m^2)}\frac{1}{((\bar{\mathbf{k}}+\frac{\Delta}{2})^2+m^2)((\bar{\mathbf{k}}-\frac{\Delta}{2})^2+m^2)}\\
&\quad\times\left[8\cos\left(\frac{\Delta}{2}\cdot\mathbf{r}\right)\cos\left(\frac{\Delta}{2}\cdot\bar{\mathbf{r}}\right)-8\cos\left(\frac{\Delta}{2}\cdot\mathbf{r}\right)\exp\left(i\bar{\mathbf{k}}\cdot\bar{\mathbf{r}}\right)-8\cos\left(\frac{\Delta}{2}\cdot\bar{\mathbf{r}}\right)\exp\left(i\mathbf{k}\cdot\mathbf{r}\right)\right.\\
&\quad\left.+4\exp\left(i\mathbf{k}\cdot\mathbf{r}+i\bar{\mathbf{k}}\cdot\bar{\mathbf{r}}\right)+4\exp\left(i\mathbf{k}\cdot\mathbf{r}-i\bar{\mathbf{k}}\cdot\bar{\mathbf{r}}\right)\right].
\end{aligned}\tag{B7}$$

Using this and the definitions (B4) and (B5) we can substitute the appropriate values for B and C. This is enough to find the color connected contributions to the Fourier transform of (B3) i.e., the average of the Fourier transformed dipole cross section squared.

Now we can write the Fourier transform of the different parts of the dipole cross section squared as

$$\begin{aligned}
&\left[\int d^2\mathbf{b}d^2\bar{\mathbf{b}}e^{-i\mathbf{b}\cdot\Delta+i\bar{\mathbf{b}}\cdot\Delta}\left\langle\!\!\left\langle\frac{d\sigma^{\mathrm{p}}_{\mathrm{dip}}}{d^2\mathbf{b}}(\mathbf{b},\mathbf{r})\frac{d\sigma^{\mathrm{p}}_{\mathrm{dip}}}{d^2\bar{\mathbf{b}}}(\bar{\mathbf{b}},\bar{\mathbf{r}})\right\rangle\!\!\right\rangle\right]_{1,DC}\\
&=\frac{g^4\mu_0^4(N_c^2-1)^2N_q}{(2\pi)^2N_c^2}\exp\left(-r_H^2\Delta^2\right)\left\{\Psi(\mathbf{r})\Psi(\bar{\mathbf{r}})+\cos\left(\frac{1}{2}\Delta\cdot\mathbf{r}\right)\cos\left(\frac{1}{2}\Delta\cdot\bar{\mathbf{r}}\right)\Psi(0)\Psi(0)\right.\\
&\quad\left.-\cos\left(\frac{1}{2}\Delta\cdot\bar{\mathbf{r}}\right)\Psi(\mathbf{r})\Psi(0)-\cos\left(\frac{1}{2}\Delta\cdot\mathbf{r}\right)\Psi(\bar{\mathbf{r}})\Psi(0)\right\}
\end{aligned}\tag{B8}$$

$$\begin{aligned}
&\left[\int d^2\mathbf{b}d^2\bar{\mathbf{b}}e^{-i\mathbf{b}\cdot\Delta+i\bar{\mathbf{b}}\cdot\Delta}\left\langle\!\!\left\langle\frac{d\sigma^{\mathrm{p}}_{\mathrm{dip}}}{d^2\mathbf{b}}(\mathbf{b},\mathbf{r})\frac{d\sigma^{\mathrm{p}}_{\mathrm{dip}}}{d^2\bar{\mathbf{b}}}(\bar{\mathbf{b}},\bar{\mathbf{r}})\right\rangle\!\!\right\rangle\right]_{2,DC}\\
&=\frac{g^4\mu_0^4(N_c^2-1)^2N_q(N_q-1)}{N_c^2(2\pi)^2}\exp\left(-(R^2+r_H^2)\Delta^2\right)\left\{\Psi(\mathbf{r})\Psi(\bar{\mathbf{r}})+\cos\left(\frac{1}{2}\Delta\cdot\mathbf{r}\right)\cos\left(\frac{1}{2}\Delta\cdot\bar{\mathbf{r}}\right)\Psi(0)\Psi(0)\right.\\
&\quad\left.-\cos\left(\frac{1}{2}\Delta\cdot\bar{\mathbf{r}}\right)\Psi(\mathbf{r})\Psi(0)-\cos\left(\frac{1}{2}\Delta\cdot\mathbf{r}\right)\Psi(\bar{\mathbf{r}})\Psi(0)\right\}
\end{aligned}\tag{B9}$$

$$\left[\int d^2\mathbf{b}d^2\bar{\mathbf{b}}e^{-i\mathbf{b}\cdot\Delta+i\bar{\mathbf{b}}\cdot\Delta}\left\langle\!\!\left\langle\frac{d\sigma^{\mathrm{p}}_{\mathrm{dip}}}{d^2\mathbf{b}}(\mathbf{b},\mathbf{r})\frac{d\sigma^{\mathrm{p}}_{\mathrm{dip}}}{d^2\bar{\mathbf{b}}}(\bar{\mathbf{b}},\bar{\mathbf{r}})\right\rangle\!\!\right\rangle\right]_{1,C}$$
$$=\frac{g^4\mu_0^4(N_c^2-1)}{64\pi^4N_c^2}N_q\int d^2\mathbf{k}d^2\bar{\mathbf{k}}\frac{\exp\left(-r_H^2(\mathbf{k}+\bar{\mathbf{k}})^2\right)}{((\mathbf{k}+\frac{\Delta}{2})^2+m^2)((\mathbf{k}-\frac{\Delta}{2})^2+m^2)}\frac{1}{((\bar{\mathbf{k}}+\frac{\Delta}{2})^2+m^2)((\bar{\mathbf{k}}-\frac{\Delta}{2})^2+m^2)}$$
$$\times\left\{8\cos\left(\frac{\Delta}{2}\cdot\mathbf{r}\right)\cos\left(\frac{\Delta}{2}\cdot\bar{\mathbf{r}}\right)-8\cos\left(\frac{\Delta}{2}\cdot\mathbf{r}\right)\exp\left(i\bar{\mathbf{k}}\cdot\bar{\mathbf{r}}\right)-8\cos\left(\frac{\Delta}{2}\cdot\bar{\mathbf{r}}\right)\exp\left(i\mathbf{k}\cdot\mathbf{r}\right)\right.$$
$$\left.+4\exp\left(i\mathbf{k}\cdot\mathbf{r}+i\bar{\mathbf{k}}\cdot\bar{\mathbf{r}}\right)+4\exp\left(i\mathbf{k}\cdot\mathbf{r}-i\bar{\mathbf{k}}\cdot\bar{\mathbf{r}}\right)\right\} \tag{B10}$$

and

$$\left[\int d^2\mathbf{b}d^2\bar{\mathbf{b}}e^{-i\mathbf{b}\cdot\Delta+i\bar{\mathbf{b}}\cdot\Delta}\left\langle\!\!\left\langle\frac{d\sigma^{\mathrm{p}}_{\mathrm{dip}}}{d^2\mathbf{b}}(\mathbf{b},\mathbf{r})\frac{d\sigma^{\mathrm{p}}_{\mathrm{dip}}}{d^2\bar{\mathbf{b}}}(\bar{\mathbf{b}},\bar{\mathbf{r}})\right\rangle\!\!\right\rangle\right]_{2,C}$$
$$=\frac{g^4\mu_0^4(N_c^2-1)}{64\pi^4N_c^2}N_q(N_q-1)\int d^2\mathbf{k}d^2\bar{\mathbf{k}}\frac{\exp\left(-(R^2+r_H^2)(\mathbf{k}+\bar{\mathbf{k}})^2\right)}{((\mathbf{k}+\frac{\Delta}{2})^2+m^2)((\mathbf{k}-\frac{\Delta}{2})^2+m^2)}\frac{1}{((\bar{\mathbf{k}}+\frac{\Delta}{2})^2+m^2)((\bar{\mathbf{k}}-\frac{\Delta}{2})^2+m^2)}$$
$$\times\left\{8\cos\left(\frac{\Delta}{2}\cdot\mathbf{r}\right)\cos\left(\frac{\Delta}{2}\cdot\bar{\mathbf{r}}\right)-8\cos\left(\frac{\Delta}{2}\cdot\mathbf{r}\right)\exp\left(i\bar{\mathbf{k}}\cdot\bar{\mathbf{r}}\right)-8\cos\left(\frac{\Delta}{2}\cdot\bar{\mathbf{r}}\right)\exp\left(i\mathbf{k}\cdot\mathbf{r}\right)\right.$$
$$\left.+4\exp\left(i\mathbf{k}\cdot\mathbf{r}+i\bar{\mathbf{k}}\cdot\bar{\mathbf{r}}\right)+4\exp\left(i\mathbf{k}\cdot\mathbf{r}-i\bar{\mathbf{k}}\cdot\bar{\mathbf{r}}\right)\right\}. \tag{B11}$$

The latter two color connected terms can be integrated over the angles of the dipole size $\mathbf{r},\bar{\mathbf{r}}$ as the nonrelativistic wave functions remove the Fourier exponent depending on the dipole orientation. This yields

$$\left[\int d\theta_{\mathbf{r}}d\theta_{\bar{\mathbf{r}}}\int d^2\mathbf{b}d^2\bar{\mathbf{b}}e^{-i\mathbf{b}\cdot\Delta+i\bar{\mathbf{b}}\cdot\Delta}\left\langle\!\!\left\langle\frac{d\sigma^{\mathrm{p}}_{\mathrm{dip}}}{d^2\mathbf{b}}(\mathbf{b},\mathbf{r})\frac{d\sigma^{\mathrm{p}}_{\mathrm{dip}}}{d^2\bar{\mathbf{b}}}(\bar{\mathbf{b}},\bar{\mathbf{r}})\right\rangle\!\!\right\rangle\right]_{1,C}$$
$$=\frac{g^4\mu_0^4(N_c^2-1)}{2\pi^2N_c^2}N_q\int d^2\mathbf{k}d^2\bar{\mathbf{k}}\frac{\exp\left(-r_H^2(\mathbf{k}+\bar{\mathbf{k}})^2\right)}{((\mathbf{k}+\frac{\Delta}{2})^2+m^2)((\mathbf{k}-\frac{\Delta}{2})^2+m^2)}\frac{1}{((\bar{\mathbf{k}}+\frac{\Delta}{2})^2+m^2)((\bar{\mathbf{k}}-\frac{\Delta}{2})^2+m^2)}$$
$$\times\left\{J_0\left(\frac{|\Delta||\mathbf{r}|}{2}\right)J_0\left(\frac{|\Delta||\bar{\mathbf{r}}|}{2}\right)-J_0\left(\frac{|\Delta||\mathbf{r}|}{2}\right)J_0(|\bar{\mathbf{k}}||\bar{\mathbf{r}}|)-J_0\left(\frac{|\Delta||\bar{\mathbf{r}}|}{2}\right)J_0(|\mathbf{k}||\mathbf{r}|)+J_0(|\mathbf{k}||\mathbf{r}|)J_0(|\bar{\mathbf{k}}||\bar{\mathbf{r}}|)\right\} \tag{B12}$$

and

$$\left[\int d\theta_{\mathbf{r}}d\theta_{\bar{\mathbf{r}}}d^2\mathbf{b}d^2\bar{\mathbf{b}}e^{-i\mathbf{b}\cdot\Delta+i\bar{\mathbf{b}}\cdot\Delta}\left\langle\!\!\left\langle\frac{d\sigma^{\mathrm{p}}_{\mathrm{dip}}}{d^2\mathbf{b}}(\mathbf{b},\mathbf{r})\frac{d\sigma^{\mathrm{p}}_{\mathrm{dip}}}{d^2\bar{\mathbf{b}}}(\bar{\mathbf{b}},\bar{\mathbf{r}})\right\rangle\!\!\right\rangle\right]_{2,C}$$
$$=\frac{g^4\mu_0^4(N_c^2-1)}{2\pi^2N_c^2}N_q(N_q-1)\int d^2\mathbf{k}d^2\bar{\mathbf{k}}\frac{\exp\left(-(R^2+r_H^2)(\mathbf{k}+\bar{\mathbf{k}})^2\right)}{((\mathbf{k}+\frac{\Delta}{2})^2+m^2)((\mathbf{k}-\frac{\Delta}{2})^2+m^2)}\frac{1}{((\bar{\mathbf{k}}+\frac{\Delta}{2})^2+m^2)((\bar{\mathbf{k}}-\frac{\Delta}{2})^2+m^2)}$$
$$\times\left\{J_0\left(\frac{|\Delta||\mathbf{r}|}{2}\right)J_0\left(\frac{|\Delta||\bar{\mathbf{r}}|}{2}\right)-J_0\left(\frac{|\Delta||\mathbf{r}|}{2}\right)J_0(|\bar{\mathbf{k}}||\bar{\mathbf{r}}|)-J_0\left(\frac{|\Delta||\bar{\mathbf{r}}|}{2}\right)J_0(|\mathbf{k}||\mathbf{r}|)+J_0(|\mathbf{k}||\mathbf{r}|)J_0(|\bar{\mathbf{k}}||\bar{\mathbf{r}}|)\right\}. \tag{B13}$$

These are now the forms of the parts of the cross section that we can convolute with the vector meson-photon overlaps and integrate over the dipole sizes. This is also the form which we can easily expand in the small-$\mathbf{r}$ limit as we do in Appendix D.

APPENDIX C: $\Delta = 0$ EXPANSION OF THE COHERENT CROSS SECTION

The Z-and K functions have a nontrivial dependence on m and Δ. To proceed further we must look at specific limits in terms of these variables. In particular we are

interested in the behavior in the limits of small and large Δ.

Using the definitions (45), (30), and (31), the coherent cross section (46) at the limit of $\Delta = 0$, or $t = 0$, can be written as

$$\left.\frac{d\sigma_{T,L}^{\gamma^* p\to Vp}}{dt}\right|_{t=0} = \frac{1}{16\pi}[C_T^2 + C_L^2]\frac{g^4\mu_0^4(N_c^2-1)^2N_q^2}{(2\pi N_c)^2} \times\left[\int d^2\mathbf{r}K_0(\varepsilon'|\mathbf{r}|)\left\{\frac{1}{2m^2}-\frac{|\mathbf{r}|K_1(m|\mathbf{r}|)}{2m}\right\}\right]^2. \tag{C1}$$

The $\mathbf{r}$-integral yields

$$\left.\frac{d\sigma_{T,L}^{\gamma^* p\to Vp}}{dt}\right|_{t=0} = \frac{1}{16\pi}[C_T^2 + C_L^2]\frac{g^4\mu_0^4(N_c^2-1)^2N_q^2}{(2\pi N_c)^2} \times\left[\frac{\pi}{m^2}\left(\frac{1}{\varepsilon'^2}-\frac{\varepsilon'^2-m^2+2m^2\log(\frac{m}{\varepsilon'})}{(\varepsilon'^2-m^2)^2}\right)\right]^2. \tag{C2}$$

Expanding this at small m to the lowest nontrivial order yields

$$\left.\frac{d\sigma_{T,L}^{\gamma^* p\to Vp}}{dt}\right|_{t=0} \approx \frac{1}{16\pi}[C_T^2 + C_L^2]\frac{g^4\mu_0^4(N_c^2-1)^2N_q^2}{(2\pi N_c)^2} \times\left[-\frac{\pi(1+2\log(\frac{m}{\varepsilon'}))}{\varepsilon'^4}\right]^2 + \mathcal{O}(m^2). \tag{C3}$$

Firstly, this limit serves as a convenient check of the numerical evaluation of the coherent cross section. Moreover, it demonstrates the important effect of the IR regulator m on the magnitude of the coherent cross section. From this expression, using $\varepsilon' \sim m_Q$ for $m_Q^2 \gg Q^2$ and the definition of the constants $C_{T,L}$ from (42) and (43) one can deduce the power-law dependence of the cross section in the heavy quark limit $d\sigma/dt \sim \Gamma_V/m_Q^5$.

APPENDIX D: THE SMALL DIPOLE SIZE EXPANSION OF THE CROSS SECTIONS

1. The small dipole size approximation

In this appendix we study the small dipole size expansion of our results. Here the argument is that for a heavy quark, we would expect the photon wave function to set $r \sim 1/m_Q$, so that both the meson wave function and the dipole amplitude can be expanded to lowest nontrivial order in r. In this limit several of the integrals that we were left with in the full case can be calculated analytically. We expand the dipole cross section Fourier transforms to the lowest nontrivial order in the dipole size $\mathbf{r}$. We keep the photon wave function contribution intact as it kills off the large dipole size contributions at a scale dependent on the quark masses and the photon virtuality.

The Fourier-transform of the coherent amplitude (29) has a small $\mathbf{r}$ expansion which reads

$$\begin{aligned}\int d^2\mathbf{b}e^{-i\mathbf{b}\cdot\Delta}\left\langle\!\!\left\langle\frac{d\sigma_{\rm dip}^{\rm p}}{d^2\mathbf{b}}(\mathbf{b},\mathbf{r})\right\rangle\!\!\right\rangle &= \frac{g^2\mu_0^2(N_c^2-1)N_q}{2\pi N_c}\exp\left\{-\frac{1}{2}\left(r_H^2+\left(\frac{N_q-1}{N_q}\right)R^2\right)\Delta^2\right\} \\ &\times\left[\frac{(\Delta\cdot\mathbf{r})^2}{4\Delta^2}\left\{-1+\frac{4m^2}{\Delta\sqrt{\Delta^2+4m^2}}\operatorname{arctanh}\left(\frac{\Delta}{\sqrt{\Delta^2+4m^2}}\right)\right\}\right. \\ &+\mathbf{r}^2\left\{-\frac{1}{4}\log(m\mathbf{r})+\frac{1}{8}\log(4e^{3-2\gamma})\right. \\ &\left.\left.-\frac{1}{4}\sqrt{1+4\frac{m^2}{\Delta^2}}\operatorname{arccoth}\left(\sqrt{1+4\frac{m^2}{\Delta^2}}\right)\right\}\right].\end{aligned} \tag{D1}$$

Here one should note that the term depending on the orientation of the dipole with respect to the momentum transfer (the $(\Delta\cdot\mathbf{r})^2$-term) does not vanish in the lowest order in the dipole size. This feature has an interpretation in terms of the Wigner distribution of the proton, and corresponds to an angular correlation between the jet axis and momentum transfer in exclusive dijet production [46–49], in particular see Appendix D of Ref. [50] for analytical results very similar to ours. However, this term vanishes in the limit of large m/Δ. This effect has an interesting interpretation in terms of the shape of the proton. When m is large, the gluon field generated by a pointlike color charge is more or less pointlike, which translates to the gluon field of the proton being Gaussian because the color charges are distributed as a Gaussian. This reduces the size of the boundary, which is where the orientation of the small dipole matters, and this makes the angle dependence vanish at the lowest order of the dipole size. On the other hand when the m is not large, the shape of the gluon field of the proton is decreasing more as a power law (in momentum space, a modified Bessel function in coordinate space), which makes the boundary more relevant than in the Gaussian shape and results in the angle dependent term having a significant contribution.

To get the small-r expressions for the cross sections, we expand the dipole cross section to the lowest nontrivial order in the dipole size r before integrating it with the wave function overlap. The small-r expressions for the Z—and K-functions defined in (45) and (50) then read

$$\begin{aligned}&Z_{\mathbf{r}\approx 0}(\Delta,m^2,\varepsilon') \\ &\equiv\frac{2\pi}{\varepsilon'^4}\left[-\frac{2m^2+\Delta^2}{\Delta\sqrt{4m^2+\Delta^2}}\operatorname{arctanh}\left(\frac{\Delta}{\sqrt{4m^2+\Delta^2}}\right)+\log\left(\frac{\varepsilon'}{m}\right)\right]\end{aligned} \tag{D2}$$

and

$$K_{\mathbf{r}\approx 0}(A,\Delta,m^2,\varepsilon') \equiv \frac{1}{\varepsilon'^8}\int d^2\mathbf{k}d^2\bar{\mathbf{k}}\,\frac{\exp\left(-A(\mathbf{k}+\bar{\mathbf{k}})^2\right)}{((\mathbf{k}+\frac{\Delta}{2})^2+m^2)((\mathbf{k}-\frac{\Delta}{2})^2+m^2)}\frac{1}{((\bar{\mathbf{k}}+\frac{\Delta}{2})^2+m^2)((\bar{\mathbf{k}}-\frac{\Delta}{2})^2+m^2)} \times\left[\frac{\Delta^4}{16}-\frac{\Delta^2\bar{\mathbf{k}}^2}{4}-\frac{\Delta^2\mathbf{k}^2}{4}+\mathbf{k}^2\bar{\mathbf{k}}^2\right]. \tag{D3}$$

We see that the Z-function, and consequently the coherent and hot spot fluctuation parts of the cross section, retain a logarithmic dependence on ε' and thus the quark mass even in the small dipole limit. Only in the color fluctuation part, i.e., the function K, the dependence on the quark mass becomes a pure power law.

In the small $\mathbf{r}/\bar{\mathbf{r}}$ limit of the dipole cross section, the coherent cross section becomes

$$\left.\frac{d\sigma_{T,L}^{\gamma^* p\to Vp}}{dt}\right|_{\mathbf{r}\approx 0} = \frac{1}{16\pi}C_{T,L}^2\frac{g^4\mu_0^4(N_c^2-1)^2N_q^2}{(2\pi N_c)^2}\exp\left(-\left[r_H^2+\left(\frac{N_q-1}{N_q}\right)R^2\right]\Delta^2\right)Z_{\mathbf{r}\approx 0}(\Delta,m^2,\varepsilon')^2. \tag{D4}$$

Now by also expanding (50), the parts of the incoherent cross section, in the small-$\mathbf{r}$ limit, read

$$\left.\frac{d\sigma_{T,L}^{\gamma^* p\to Vp^*}}{dt}\right|_{1,DC,\mathbf{r}\approx 0} = \frac{1}{16\pi}C_{T,L}^2\frac{g^4\mu_0^4(N_c^2-1)^2}{(2\pi N_c)^2}N_q\left[\exp\left(-\Delta^2 r_H^2\right)-\exp\left(-\left[r_H^2+\left(\frac{N_q-1}{N_q}\right)R^2\right]\Delta^2\right)\right]Z_{\mathbf{r}\approx 0}(\Delta,m^2,\varepsilon')^2, \tag{D5}$$

$$\left.\frac{d\sigma_{T,L}^{\gamma^* p\to Vp^*}}{dt}\right|_{2,DC,\mathbf{r}\approx 0} = \frac{1}{16\pi}C_{T,L}^2\frac{g^4\mu_0^4(N_c^2-1)^2}{(2\pi N_c)^2}N_q(N_q-1)\left[\exp\left(-\Delta^2[R^2+r_H^2]\right)-\exp\left(-\left[r_H^2+\left(\frac{N_q-1}{N_q}\right)R^2\right]\Delta^2\right)\right] \times Z_{\mathbf{r}\approx 0}(\Delta,m^2,\varepsilon')^2, \tag{D6}$$

$$\left.\frac{d\sigma_{T,L}^{\gamma^* p\to Vp^*}}{dt}\right|_{1,C,\mathbf{r}\approx 0} = \frac{1}{16\pi}C_{T,L}^2\frac{g^4\mu_0^4(N_c^2-1)}{2\pi^2N_c^2}N_qK_{\mathbf{r}\approx 0}(r_H^2,\Delta,m^2,\varepsilon'), \tag{D7}$$

$$\left.\frac{d\sigma_{T,L}^{\gamma^* p\to Vp^*}}{dt}\right|_{2,C,\mathbf{r}\approx 0} = \frac{1}{16\pi}C_{T,L}^2\frac{g^4\mu_0^4(N_c^2-1)}{2\pi^2N_c^2}N_q(N_q-1)K_{\mathbf{r}\approx 0}(R^2+r_H^2,\Delta,m^2,\varepsilon'), \tag{D8}$$

where the subscripts are the same as before, referring to the number of hot spots and whether the color structure is connected or not.

2. Small-r coherent cross section at $\Delta=\infty$ and $\Delta=0$

The small-$\mathbf{r}$ limit of the coherent cross section reads

$$\frac{d\sigma_{T,L}^{\gamma^* p\to Vp}}{dt} = \frac{1}{16\pi}C_{T,L}^2\frac{g^4\mu_0^4(N_c^2-1)^2N_q^2}{N_c^2\varepsilon'^8}\exp\left(-\left[r_H^2+\left(\frac{N_q-1}{N_q}\right)R^2\right]\Delta^2\right)\left[-\frac{2m^2+\Delta^2}{\Delta\sqrt{4m^2+\Delta^2}}\operatorname{arctanh}\left(\frac{\Delta}{\sqrt{4m^2+\Delta^2}}\right)+\log\left(\frac{\varepsilon'}{m}\right)\right]^2. \tag{D9}$$

Now to approximate this at large t, we expand the function in the square brackets in large $-t=\Delta^2$. This yields

$$\left.\frac{d\sigma_{T,L}^{\gamma^* p\to Vp}}{dt}\right|_{-t\to\infty} = \frac{1}{16\pi}C_{T,L}^2\frac{g^4\mu_0^4(N_c^2-1)^2N_q^2}{N_c^2\varepsilon'^8}\exp\left(\left[r_H^2+\left(\frac{N_q-1}{N_q}\right)R^2\right]t\right)\frac{1}{4}\log\left(\frac{\varepsilon'^2}{-t}\right)^2. \tag{D10}$$

This result also coincides with the small-m expansion of (D9).

On the other hand, we can approximate the slope at $-t=\Delta^2=0$ by first expanding the square bracket at small t. Doing this we get

$$\left.\frac{d\sigma_{T,L}^{\gamma^* p\to Vp}}{dt}\right|_{t\approx 0} = \frac{1}{16\pi}C_{T,L}^2\frac{g^4\mu_0^4(N_c^2-1)^2N_q^2}{N_c^2\varepsilon'^8}\exp\left(\left[r_H^2+\left(\frac{N_q-1}{N_q}\right)R^2\right]t\right)\left(\log\left(\frac{\varepsilon'}{m}\right)-\frac{1}{2}\right)^2\left[1-\frac{-t}{3m^2(\log(\frac{\varepsilon'}{m})-\frac{1}{2})}\right]. \tag{D11}$$

Near $t=0$ we can use this to get an expression that is an exponential in t, but with a slope that takes into account the Coulomb tails regulated by m.

$$\left.\frac{d\sigma_{T,L}^{\gamma^* p\to Vp}}{dt}\right|_{t\approx 0} = \frac{1}{16\pi} C_{T,L}^2 \frac{g^4\mu_0^4 (N_c^2-1)^2 N_q^2}{N_c^2 \varepsilon'^8}\left(\log\left(\frac{\varepsilon'}{m}\right)-\frac{1}{2}\right)^2 \times \exp\left(\left[r_H^2+\left(\frac{N_q-1}{N_q}\right)R^2+\frac{1}{3m^2(\log(\frac{\varepsilon'}{m})-\frac{1}{2})}\right]t\right). \tag{D12}$$

For a finite IR regulator m, the correction to the slope $\sim 1/[m^2\log(m_Q/m)]$ does indeed vanish in the limit $m_Q\to\infty$, but this happens only extremely slowly. Note also that this reexponentiation that gives an interpretation as a correction to the coherent slope is based in an expansion in t/m^2, and is thus valid for only very small values of t.

3. Large-t behavior of the small-r incoherent cross section

In the large t limit the incoherent cross section is dominated by the color fluctuation contributions. For this we need to look at the large t behavior of the integral

$$\int d^2\mathbf{k} d^2\bar{\mathbf{k}} \frac{\exp\left(-A(\mathbf{k}+\bar{\mathbf{k}})^2\right)}{((\mathbf{k}+\frac{\Delta}{2})^2+m^2)((\mathbf{k}-\frac{\Delta}{2})^2+m^2)} \times \frac{1}{((\bar{\mathbf{k}}+\frac{\Delta}{2})^2+m^2)((\bar{\mathbf{k}}-\frac{\Delta}{2})^2+m^2)} \times \left[\frac{\Delta^4}{16}-\frac{\Delta^2\bar{\mathbf{k}}^2}{4}-\frac{\Delta^2\mathbf{k}^2}{4}+\mathbf{k}^2\bar{\mathbf{k}}^2\right], \tag{D13}$$

with $A=R^2+r_H^2$ for the two hot spot case and $A=r_H^2$ for the one hot spot case. Here the former has a much smaller effect for the large-t tail, as we shall see.

Firstly let us change the coordinates to $\mathbf{q}=\mathbf{k}+\bar{\mathbf{k}}$ and $\bar{\mathbf{q}}=\mathbf{k}-\bar{\mathbf{k}}$. Doing this, and by simplifying a bit, we get

$$=4\int d^2\mathbf{q} d^2\bar{\mathbf{q}} \frac{\exp\left(-A\mathbf{q}^2\right)}{((\mathbf{q}+\bar{\mathbf{q}}+\Delta)^2+4m^2)((\mathbf{q}+\bar{\mathbf{q}}-\Delta)^2+4m^2)} \times \frac{1}{((\mathbf{q}-\bar{\mathbf{q}}+\Delta)^2+4m^2)((\mathbf{q}-\bar{\mathbf{q}}-\Delta)^2+4m^2)} \times [\Delta^4-\Delta^2(\mathbf{q}-\bar{\mathbf{q}})^2-\Delta^2(\mathbf{q}+\bar{\mathbf{q}})^2+(\mathbf{q}+\bar{\mathbf{q}})^2(\mathbf{q}-\bar{\mathbf{q}})^2]. \tag{D14}$$

Now by assuming that the Gaussian restricts $\mathbf{q}$ to small values, we can set $\mathbf{q}=0$ everywhere else. Performing the Gaussian integration, we get

$$=\frac{4\pi}{A}\int d^2\bar{\mathbf{q}} \frac{\Delta^4-2\Delta^2\bar{\mathbf{q}}^2+\bar{\mathbf{q}}^4}{((\bar{\mathbf{q}}+\Delta)^2+4m^2)^2((\bar{\mathbf{q}}-\Delta)^2+4m^2)^2}. \tag{D15}$$

The angle of Δ does not matter in our calculation so we can choose Δ to be fully in the x direction. This integration can be performed in the Cartesian coordinates, and it yields

$$=-\frac{\pi^2}{2A\Delta^3}\left[\frac{2(4m^4\Delta+2m^2\Delta^3+\Delta^5)}{(4m^2+\Delta^2)^2} - \frac{4(8m^6+16m^4\Delta^2+6m^2\Delta^4+\Delta^6)\operatorname{arctanh}(\frac{\Delta}{\sqrt{4m^2+\Delta^2}})}{(4m^2+\Delta^2)^{\frac{5}{2}}}\right]. \tag{D16}$$

Now expanding this to the leading order at large Δ, we get

$$\approx -\frac{\pi^2(1+\log(\frac{m^2}{\Delta^2}))}{A\Delta^2}+\mathcal{O}\left(\frac{1}{\Delta^4}\right). \tag{D17}$$

We can also write this as

$$\approx \frac{\pi^2(1+\log(-\frac{m^2}{t}))}{At}+\mathcal{O}\left(\frac{1}{t^2}\right). \tag{D18}$$

Now it is clear that the smaller A term with $A=r_H^2$ dominates over the $A=R^2+r_H^2$ one. Thus, setting $A=r_H^2$ in Eq. (D18) gives the large-t limit for the incoherent cross section.

4. Comparing the full result with the analytical limits

In Fig. 7 we have plotted the cross sections for both the full and small-r expressions together with their expected behavior in the different regimes. For the coherent cross section we have plotted the full result (2), its small-$\mathbf{r}$ expansion (D4), an exponential $\propto\exp(tR_C^2)$ with the coherent radius (28) and the two limits where we approximate the t behavior with exponentials obtained from the slope of the small-$\mathbf{r}$ expansion at $\Delta=0$ (D12) and $\Delta=\infty$ (D10). In these plots we use the actual normalizations of the limits as they are seen in the equations.

Firstly looking at the charm quark coherent cross sections, we see that both the full and the small-r cross sections stray from both the expected exponential and from each other already at small $|t|$. We also see a dip in the small-$\mathbf{r}$ limit of the coherent cross section. This dip appears because the $Z_{\mathbf{r}\approx 0}$-function changes sign. It also exists for the heavier quarks but its location is at a higher value of t the higher the quark mass m_Q, or photon virtuality Q^2, is. We see that in the range of t we study here, the bottom quark mass is sufficient to make the full and small-$\mathbf{r}$ results of the coherent cross section coincide quite well. Also the $t=\infty$ limit expansion of the coherent cross section works

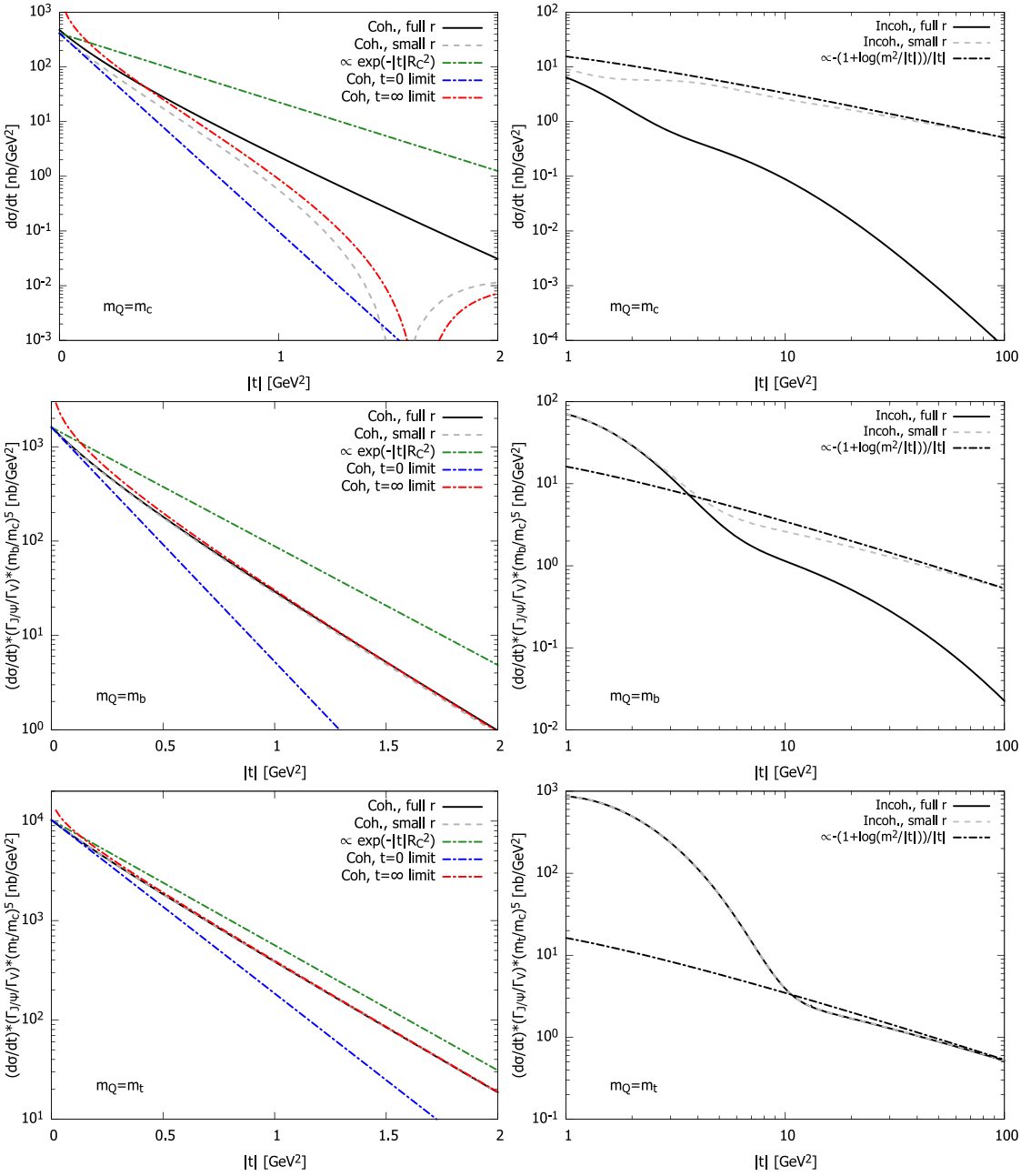

FIG. 7. Comparison of the analytic small-r limits of the coherent (D4) and incoherent cross sections (D5), (D6), (D7), and (D8) to the full numerical result. Also shown are analytical results obtained in the small or large t limits, Eqs. (D12), (D10), and (D17) and an exponential with a value at $t = 0$, which can be easily seen from Eq. (D11) by setting $t = 0$, and a slope given by the coherent radius. As usual, the top row shows the result for the c mass, the middle row for b and the bottom row for t.

quite well except for the very low t values. For the top quark case, we see that both the full and the small-$\mathbf{r}$ coherent cross sections almost have the expected exponential decay and thus measure the overall size of the proton much better than the c and b quarks. The $t = 0$ limit expansion of the coherent cross section does not work very well for any of the quark masses except at very low values of t.

Next let us look at the incoherent cross section. In Fig. 7 we have also plotted the full incoherent cross section (48), (49), (51), and (52), the small-$\mathbf{r}$ expansion of the incoherent cross section (D5), (D6), (D7), (D8), and the small-$\mathbf{r}$ and large-t expansion of the incoherent cross section [(D7) with the integral substituted with (D17)]. Also, here we use also the normalization resulting from the calculation in the plot.

Firstly we notice that for the charm quark, the small-$\mathbf{r}$ incoherent cross section goes down much too slowly in comparison to the full-$\mathbf{r}$ result. The large-t expansion does

capture the behavior of the small-**r** limit of the incoherent cross section, however. We seem to have to have extremely heavy quarks to make the dipole size to be small enough to warrant for the small-**r** expansion. This can be seen in the bottom quark plot where the mass of this quark is not high enough to really make the expansion work. Only in the top quark case do we see that our small-**r** limit is the correct one for the asymptotically heavy quark limit.

[1] A. Aktas *et al.* (H1 Collaboration), Elastic J/ψ production at HERA, Eur. Phys. J. C **46**, 585 (2006).

[2] A. Aktas *et al.* (H1 Collaboration), Diffractive photoproduction of J/ψ mesons with large momentum transfer at HERA, Phys. Lett. B **568**, 205 (2003).

[3] C. Alexa *et al.* (H1 Collaboration), Elastic and proton-dissociative photoproduction of J/ψ mesons at HERA, Eur. Phys. J. C **73**, 2466 (2013).

[4] J. Breitweg *et al.* (ZEUS Collaboration), Measurement of diffractive photoproduction of vector mesons at large momentum transfer at HERA, Eur. Phys. J. C **14**, 213 (2000).

[5] S. Chekanov *et al.* (ZEUS Collaboration), Measurement of proton dissociative diffractive photoproduction of vector mesons at large momentum transfer at HERA, Eur. Phys. J. C **26**, 389 (2003).

[6] A. J. Baltz, The physics of ultraperipheral collisions at the LHC, Phys. Rep. **458**, 1 (2008).

[7] S. Klein *et al.*, New opportunities at the photon energy frontier, arXiv:2009.03838.

[8] A. Accardi *et al.*, Electron ion collider: The next QCD frontier: Understanding the glue that binds us all, Eur. Phys. J. A **52**, 268 (2016).

[9] R. Abdul Khalek *et al.*, Science requirements and detector concepts for the electron-ion collider: EIC yellow report, Nucl. Phys. **A1026**, 122447 (2022).

[10] R. Abdul Khalek *et al.*, in 2022 Snowmass Summer Study (2022), arXiv:2203.13199.

[11] A. Bzdak, B. Schenke, P. Tribedy, and R. Venugopalan, Initial state geometry and the role of hydrodynamics in proton-proton, proton-nucleus and deuteron-nucleus collisions, Phys. Rev. C **87**, 064906 (2013).

[12] B. Schenke and R. Venugopalan, Eccentric Protons? Sensitivity of Flow to System Size and Shape in $p+p$, $p+\mathrm{Pb}$ and $\mathrm{Pb}+\mathrm{Pb}$ Collisions, Phys. Rev. Lett. **113**, 102301 (2014).

[13] J. L. Albacete and A. Soto-Ontoso, Hot spots and the hollowness of proton–proton interactions at high energies, Phys. Lett. B **770**, 149 (2017).

[14] J. L. Albacete, H. Petersen, and A. Soto-Ontoso, Correlated wounded hot spots in proton-proton interactions, Phys. Rev. C **95**, 064909 (2017).

[15] R. D. Weller and P. Romatschke, One fluid to rule them all: viscous hydrodynamic description of event-by-event central $p+p$, $\mathrm{p}+\mathrm{Pb}$ and $\mathrm{Pb}+\mathrm{Pb}$ collisions at $\sqrt{s}=5.02$ TeV, Phys. Lett. B **774**, 351 (2017).

[16] H. Mäntysaari, B. Schenke, C. Shen, and P. Tribedy, Imprints of fluctuating proton shapes on flow in proton-lead collisions at the LHC, Phys. Lett. B **772**, 681 (2017).

[17] J. S. Moreland, J. E. Bernhard, and S. A. Bass, Bayesian calibration of a hybrid nuclear collision model using p-Pb and Pb-Pb data at energies available at the CERN Large Hadron Collider, Phys. Rev. C **101**, 024911 (2020).

[18] H. Mäntysaari, Review of proton and nuclear shape fluctuations at high energy, Rep. Prog. Phys. **83**, 082201 (2020).

[19] S. Schlichting and B. Schenke, The shape of the proton at high energies, Phys. Lett. B **739**, 313 (2014).

[20] H. Mäntysaari and B. Schenke, Evidence of Strong Proton Shape Fluctuations from Incoherent Diffraction, Phys. Rev. Lett. **117**, 052301 (2016).

[21] H. Mäntysaari and B. Schenke, Revealing proton shape fluctuations with incoherent diffraction at high energy, Phys. Rev. D **94**, 034042 (2016).

[22] H. Mäntysaari and B. Schenke, Probing subnucleon scale fluctuations in ultraperipheral heavy ion collisions, Phys. Lett. B **772**, 832 (2017).

[23] H. Mäntysaari and B. Schenke, Confronting impact parameter dependent JIMWLK evolution with HERA data, Phys. Rev. D **98**, 034013 (2018).

[24] M. C. Traini and J.-P. Blaizot, Diffractive incoherent vector meson production off protons: A quark model approach to gluon fluctuation effects, Eur. Phys. J. C **79**, 327 (2019).

[25] A. Kumar and T. Toll, Investigating the structure of gluon fluctuations in the proton with incoherent diffraction at HERA, Eur. Phys. J. C **82**, 837 (2022).

[26] S. Demirci, T. Lappi, and S. Schlichting, Hot spots and gluon field fluctuations as causes of eccentricity in small systems, Phys. Rev. D **103**, 094025 (2021).

[27] F. Salazar, B. Schenke, and A. Soto-Ontoso, Accessing subnuclear fluctuations and saturation with multiplicity dependent J/ψ production in $p+p$ and $\mathrm{p}+\mathrm{Pb}$ collisions, Phys. Lett. B **827**, 136952 (2022).

[28] H. Mäntysaari, B. Schenke, C. Shen, and W. Zhao, Bayesian inference of the fluctuating proton shape, Phys. Lett. B **833**, 137348 (2022).

[29] A. Dumitru and R. Paatelainen, Sub-femtometer scale color charge fluctuations in a proton made of three quarks and a gluon, Phys. Rev. D **103**, 034026 (2021).

[30] A. Dumitru, H. Mäntysaari, and R. Paatelainen, Color charge correlations in the proton at NLO: Beyond geometry based intuition, Phys. Lett. B **820**, 136560 (2021).

[31] F. Gelis, E. Iancu, J. Jalilian-Marian, and R. Venugopalan, The color glass condensate, Annu. Rev. Nucl. Part. Sci. **60**, 463 (2010).

[32] L. D. McLerran and R. Venugopalan, Computing quark and gluon distribution functions for very large nuclei, Phys. Rev. D **49**, 2233 (1994).

[33] L. D. McLerran and R. Venugopalan, Gluon distribution functions for very large nuclei at small transverse momentum, Phys. Rev. D **49**, 3352 (1994).
[34] L. D. McLerran and R. Venugopalan, Green's functions in the color field of a large nucleus, Phys. Rev. D **50**, 2225 (1994).
[35] H. Kowalski, L. Motyka, and G. Watt, Exclusive diffractive processes at HERA within the dipole picture, Phys. Rev. D **74**, 074016 (2006).
[36] T. Lappi, H. Mäntysaari, and J. Penttala, Relativistic corrections to the vector meson light front wave function, Phys. Rev. D **102**, 054020 (2020).
[37] M. L. Good and W. D. Walker, Diffraction disssociation of beam particles, Phys. Rev. **120**, 1857 (1960).
[38] H. I. Miettinen and J. Pumplin, Diffraction scattering and the parton structure of hadrons, Phys. Rev. D **18**, 1696 (1978).
[39] T. Lappi and H. Mantysaari, Incoherent diffractive J/Ψ-production in high energy nuclear DIS, Phys. Rev. C **83**, 065202 (2011).
[40] C. Marquet and H. Weigert, New observables to test the Color Glass Condensate beyond the large- N_c limit, Nucl. Phys. **A843**, 68 (2010).
[41] Y. Hatta, B.-W. Xiao, and F. Yuan, Gluon tomography from deeply virtual compton scattering at small-x, Phys. Rev. D **95**, 114026 (2017).
[42] A. Kovner and U. A. Wiedemann, Eikonal evolution and gluon radiation, Phys. Rev. D **64**, 114002 (2001).
[43] A. Caldwell and H. Kowalski, Investigating the gluonic structure of nuclei via J/ψ scattering, Phys. Rev. C **81**, 025203 (2010).
[44] F. Dominguez, C. Marquet, and B. Wu, On multiple scatterings of mesons in hot and cold QCD matter, Nucl. Phys. **A823**, 99 (2009).
[45] C. Marquet and B. Wu, in *Proceedings of the 17th International Workshop on Deep-Inelastic Scattering and Related Subjects* (2009), p. 176, arXiv:0908.4180.
[46] Y. Hatta, B.-W. Xiao, and F. Yuan, Probing the Small- x Gluon Tomography in Correlated Hard Diffractive Dijet Production in Deep Inelastic Scattering, Phys. Rev. Lett. **116**, 202301 (2016).
[47] T. Altinoluk, N. Armesto, G. Beuf, and A. H. Rezaeian, Diffractive dijet production in deep inelastic scattering and photon-hadron collisions in the color glass condensate, Phys. Lett. B **758**, 373 (2016).
[48] H. Mäntysaari, N. Mueller, and B. Schenke, Diffractive dijet production and wigner distributions from the color glass condensate, Phys. Rev. D **99**, 074004 (2019).
[49] H. Mäntysaari, K. Roy, F. Salazar, and B. Schenke, Gluon imaging using azimuthal correlations in diffractive scattering at the Electron-Ion Collider, Phys. Rev. D **103**, 094026 (2021).
[50] F. Salazar and B. Schenke, Diffractive dijet production in impact parameter dependent saturation models, Phys. Rev. D **100**, 034007 (2019).